

Quantifying Carbon Cycle Extremes and Attributing Their Causes Under Climate and Land Use & Land Cover Change from 1850 to 2300

Bharat Sharma^{1,2}, Jitendra Kumar³, Nathan Collier², and
Auroop R. Ganguly¹, Forrest M. Hoffman^{2,4}

¹Sustainability and Data Sciences Laboratory, Department of Civil and Environmental Engineering,
Northeastern University, Boston, Massachusetts, USA

²Computational Sciences & Engineering Division and the Climate Change Science Institute, Oak Ridge National Laboratory, Oak Ridge, Tennessee, USA

⁴Department of Civil and Environmental Engineering, University of Tennessee, Knoxville, Tennessee, USA

Key Points:

- Human activities, through land-use change, lead to increased intensity, duration, and frequency of negative extremes in GPP.
 - Precipitation anomaly is the dominant trigger for GPP extremes, while soil moisture anomaly leads to extended extreme events.
 - The regions with overall reduction in GPP often show weakening of negative extremes in GPP

This manuscript has been authored by UT-Battelle, LLC, under contract DE-AC05-00OR22725 with the US Department of Energy (DOE). The US government retains and the publisher, by accepting the article for publication, acknowledges that the US government retains a nonexclusive, paid-up, irrevocable, worldwide license to publish or reproduce the published form of this manuscript, or allow others to do so, for US government purposes. DOE will provide public access to these results of federally sponsored research in accordance with the DOE Public Access Plan (<http://energy.gov/downloads/doe-public-access-plan>).

Corresponding author: Bharat Sharma, bharat.sharma.neu@gmail.com

Abstract

The increasing atmospheric CO₂ mole fraction affects global climate through radiative (trapping longwave radiation) and physiological effects (reduction of plant transpiration). We use the simulations of the Community Earth System Model (CESM1-BGC) forced with Representative Concentration Pathway 8.5 to investigate climate-vegetation feedbacks from 1850 to the year 2300. Human-induced land use and land cover change (LULCC), through biogeochemical and biogeophysical processes, alter the climate and modify photosynthetic activity. The changing characteristics of extreme anomalies in photosynthesis, referred to as carbon cycle extremes, increase the uncertainty of terrestrial ecosystems to act as a net carbon sink. However, the role of LULCC in altering carbon cycle extremes under business-as-usual (continuously rising) CO₂ emissions is unknown. Here we show that LULCC magnifies the intensity, frequency, and extent of carbon cycle extremes, resulting in a net reduction in expected photosynthetic activity in the future. We found that large temporally contiguous negative carbon cycle extremes are due to a persistent decrease in soil moisture, which is triggered by declines in precipitation. With LULCC and global warming, vegetation exhibits increased vulnerability to hot and dry environmental conditions, increasing the frequency of fire events and resulting in considerable losses in photosynthetic activity. While most regions show strengthening of negative carbon cycle extremes, a few locations show a weakening effect driven by declining vegetation cover or benign climate conditions for photosynthesis. Increasing hot, dry, and fire-driven carbon cycle extremes are essential for improving carbon cycle modeling and estimation of ecosystem responses to LULCC and rising CO₂ mole fractions. Moreover, large aberrations in vegetation productivity represent potential and growing threats to human lives, wildlife, and food security.

Plain Language Summary

Rising carbon dioxide (CO₂) emissions due to human activities, such as fossil fuel burning and land use and land cover change (LULCC), are the major driver of climate change. Heatwaves, droughts, and fires have increased and are expected to accelerate with climate change in the twenty-first century and beyond. This increase in extreme climate conditions has the potential to further alter vegetation productivity (called gross primary production or GPP) and carbon uptake capacity. Here, we use a global Earth system model to investigate the impacts of (1) CO₂ forcing and (2) CO₂ and LULCC forcing

on the intensity, frequency, and duration of extreme events in GPP. We found that the negative extremes in GPP, which are associated with higher losses in carbon uptake than expected, increase at a higher rate than positive GPP extremes; and this rate rises with LULCC forcing. The most dominant climate driver causing the GPP extremes is soil moisture anomalies, which are triggered by extremes in precipitation and temperature. The lagged responses of climate drivers on GPP extremes vary with the drivers and spatial location. The largest number of GPP extremes were driven by the compound effect of water-, temperature-, and fire-related drivers.

1 Introduction

Human activities are altering the Earth's atmosphere, ocean, and land surfaces at a scale and magnitude not seen throughout the past multiple thousands of years. The rising concentration of greenhouse gases (GHGs) such as water vapor, ozone, carbon dioxide, methane, and nitrous oxide are primary drivers of global warming and climate change. As a result of continued growth in the global population, the demand for fossil fuels, crops, and wood is increasing. Enhanced emissions through use of fossil fuels (*Le Quéré et al.*, 2018) and land use and land cover change (LULCC) increases the atmospheric concentration of carbon dioxide (CO₂). Rising CO₂ emissions have led to increased climate variability and frequency of climate extremes, which have a large impact on terrestrial gross primary productivity (GPP) and GPP extremes (*Marcolla et al.*, 2020; *Xian et al.*, 2020; *Reichstein et al.*, 2013; *Frank et al.*, 2015; *Ichii et al.*, 2005; *Piao et al.*, 2020). While climate extremes are relatively easy to measure, their impact on terrestrial vegetation is less detectable (*Zscheischler et al.*, 2014). Since terrestrial ecosystems absorb a quarter of anthropogenic CO₂ emissions (*Le Quéré et al.*, 2018), large changes in vegetation productivity could alter the global carbon budget. Hence, it is crucial to investigate extreme anomalies in terrestrial carbon cycle and estimate their impacts on the terrestrial carbon sink under rising CO₂ emissions and LULCC scenarios.

Prior studies (*Zhu et al.*, 2016; *Reichstein et al.*, 2013; *Bonan*, 2015) have found that the combined effect of CO₂ fertilization, increasing temperature, nitrogen deposition, and lengthening of growing seasons lead to increased vegetation productivity and strengthening of carbon sinks with a negative feedback to climate change. However, coupled carbon-climate models have large uncertainties in future projections of ecosystem responses and feedback strength (*Hoffman et al.*, 2014; *Reichstein et al.*, 2013; *Frank et al.*,

84 2015; Ichii *et al.*, 2005). Hoffman *et al.* (2014) found persistent atmospheric CO₂ biases
85 in Coupled Model Intercomparison Project 5 (CMIP5) models because of uncertainties
86 in biological and physical processes related to carbon accumulation. While most Earth
87 system model-based climate change studies analyze projections till year 2100, these pro-
88 jections may miss physical-biogeochemical feedbacks that arise later from the cumula-
89 tive effects of climate warming (Moore *et al.*, 2018). The negative sensitivity of terres-
90 trial carbon cycle to rising temperature will likely have increasing adverse implications
91 on carbon cycle extremes over time (Hubau *et al.*, 2020; Frank *et al.*, 2015). Understand-
92 ing the direction and strength of these feedbacks is essential for estimating long-term CO₂
93 concentrations and predicting and mitigating the impact and extent of climate change.
94 These limitations could alter the assessment of the rate of increase of atmospheric CO₂
95 and intensity of associated feedbacks with the terrestrial biosphere.

96 While the effects of increased warming due to greenhouse gases are spatially ex-
97 tendsive, the LULCC effects are more regional (Pitman *et al.*, 2012). The land-use his-
98 tory reconstruction used in this study estimated the proportion of land surface impacted
99 by human activities to be 60% of total vegetated area, mainly due to conversions from
100 primary vegetation to managed vegetation by 2100 (Hurtt *et al.*, 2011). The conversion
101 of land from natural to managed ecosystems reduces the carbon sink and its capacity
102 to uptake anthropogenic CO₂ and influences climate by modifying biogeophysical and
103 biogeochemical processes (Bonan *et al.*, 2012a). Changes in the plant functional type (PFT)
104 at any grid cell modifies the distribution of above and below ground carbon (Oleson *et al.*,
105 2010), response to light and energy (Bonan *et al.*, 2011), distribution of soil organic mat-
106 ter and nutrients (Koven *et al.*, 2013). Human activities, such as the conversion of forests
107 and grasslands to agricultural land and urbanization, alter net radiation, sensible and
108 latent heat partitioning, biogeochemical cycles, and the hydrologic cycle. Reduction of
109 temperate vegetation cover by deforestation increases the albedo of the surface which
110 decreases the net radiation that drives surface cooling and reduces evapotranspiration
111 that may result in declines in precipitation; but tropical deforestation for pastures de-
112 creases the total atmospheric column heating and atmospheric vertical motion which leads
113 to a warmer and drier climate (Bonan *et al.*, 2012a; Bonan, 2015). Since interannual vari-
114 ability (IAV) in GPP is strongly influenced by interannual variations in radiation, tem-
115 perature, and precipitation (Ichii *et al.*, 2005), the impact of LULCC in addition to CO₂
116 on carbon cycle extremes will likely increase over time.

Recent studies have investigated the characteristics of extreme anomalies in GPP due to climate change until the year 2100 (*Zscheischler et al.*, 2014; *Frank et al.*, 2015; *Flach et al.*, 2020; *Reichstein et al.*, 2013) and a few concluded that losses in carbon uptake due to negative extremes in GPP are compensated by increased CO₂ fertilization (*Zscheischler et al.*, 2014; *Reichstein et al.*, 2013). However, to our knowledge, no study has examined the extreme anomalies in carbon cycle beyond 2100 and the role of human LULCC in modifying carbon cycle extremes.

Rising CO₂ and LULCC impacts many components of terrestrial carbon cycle, namely total ecosystem carbon, net biome productivity, net ecosystem productivity, net primary productivity, and GPP. The overarching goal of this study is to investigate the role of CO₂ and LULCC in modifying the characteristics of extremes in one of the components, Gross Primary Productivity (GPP), and attribute changes to individual and compound effects of climate drivers. We hypothesize that 1) rising CO₂ emissions will lead to larger increases in the intensity, frequency and duration of negative carbon cycle extremes than positive extremes; and 2) LULCC activities in addition to CO₂ emissions will further increase GPP interannual variability and magnitude of carbon cycle extremes though total GPP will reduce. We performed analysis to 1) examine the magnitude, duration, frequency and spatial distribution of negative and positive carbon cycle extremes; 2) investigate the lagged response of antecedent climate drivers (and their compound effect) that drive carbon cycle extremes; 3) analyze the climate conditions that trigger long duration temporally continuous extremes; and 4) inspect regional changes in climate-carbon feedbacks for the Central and South American tropics.

2 Data

We used simulations of the Community Earth System Model (version 1) with biogeochemistry enabled, CESM1(BGC), at approximately 1° × 1° resolution to analyze climate-driven extreme anomalies in total photosynthetic activity. CESM1(BGC) is a fully coupled global climate model composed of land, atmosphere, and ocean components (*Lindsay et al.*, 2014; *Lawrence et al.*, 2012). The atmospheric CO₂ forcing time series consisted of the historical (1850–2005), Representative Concentration Pathway 8.5 (RCP 8.5; 2006–2100), and Extended Concentration Pathway (ECP 8.5; 2101–2300) mole fractions, which increased from 285 ppm in 1850 to 1962 ppm in 2300 (Figure 1(a)). Analysis of the Coupled Model Intercomparison Project 5 (CMIP5) models using the International

149 Land Model Benchmarking (ILAMB) (*Collier et al.*, 2018) show (Table S1) that CESM1(BGC)
 150 is one of the best performing model in terms of overall and IAV benchmark scores when
 151 compared to observational benchmarks.

152 We analyzed terrestrial carbon cycle extremes (or GPP extremes) using two sim-
 153 ulations, namely, *with* and *without LULCC*. In the simulation *without LULCC*, the land
 154 cover was fixed at pre-industrial (year 1850) values. In the *with LULCC* simulation, tran-
 155 sient land cover was prescribed over the historical and RCP 8.5 period (1850–2100) (*Hurtt*
 156 *et al.* (2011)) and consists of the prescribed spatial distribution of PFTs (*Lawrence et al.*
 157 (2012)). Land-use conversion is assumed to stop at the year 2100, and the distribution
 158 of PFTs remains constant at year 2100 level for the period 2100 – 2300, while wood har-
 159 vest is maintained at a constant rate over that period (*Mahowald et al.*, 2017). The re-
 160 active nitrogen deposition followed the spatially variable time series from 1850 to 2100
 161 (*Lamarque et al.*, 2010) and was subsequently held constant from 2100 to 2300. Biogeo-
 162 chemical processes on land and in the ocean respond to the historical and prescribed RCP 8.5
 163 and ECP 8.5 atmospheric CO₂ concentration forcing (Figure 1(a)). Increasing CO₂ fer-
 164 tilization, water-use efficiency, and lengthening of growing seasons enhance total pho-
 165 tosynthesis and gross primary production (GPP). These processes will be further altered
 166 by the changes in PFT distribution under *with LULCC*. Figure 1(c) shows the 5 year mov-
 167 ing average of global annually integrated GPP for simulations *with* and *without LULCC*,
 168 both forced with the same atmospheric CO₂ concentration trajectory (Figure 1(a)). The
 169 magnitude of the average GPP *with LULCC* is less than the average GPP *without LULCC*
 170 potentially due to the conversion of primary vegetation to managed vegetation.

171 3 Methods

172 A significant deviation from the mean value is called an extreme. Extreme events
 173 in GPP signify large variations in photosynthetic activity, with positive extremes rep-
 174 resenting increases in carbon uptake, while negative extremes being indicative of loss of
 175 carbon uptake (*Zscheischler et al.*, 2014). While extremes in climate have been exten-
 176 sively studied (*Reichstein et al.*, 2013; *Seneviratne and Hauser*, 2020; *Ban et al.*, 2015;
 177 *Frank et al.*, 2015; *Flach et al.*, 2020), few studies have focused on extremes in GPP and
 178 their underlying drivers(*Zscheischler et al.*, 2014; *Xu et al.*, 2019; *Flach et al.*, 2020). In
 179 this study, we identify extremes in global carbon uptake by computing percentile-based
 180 thresholds (*Seneviratne et al.*, 2012). Described in detail in Section 3.1, a positive (or

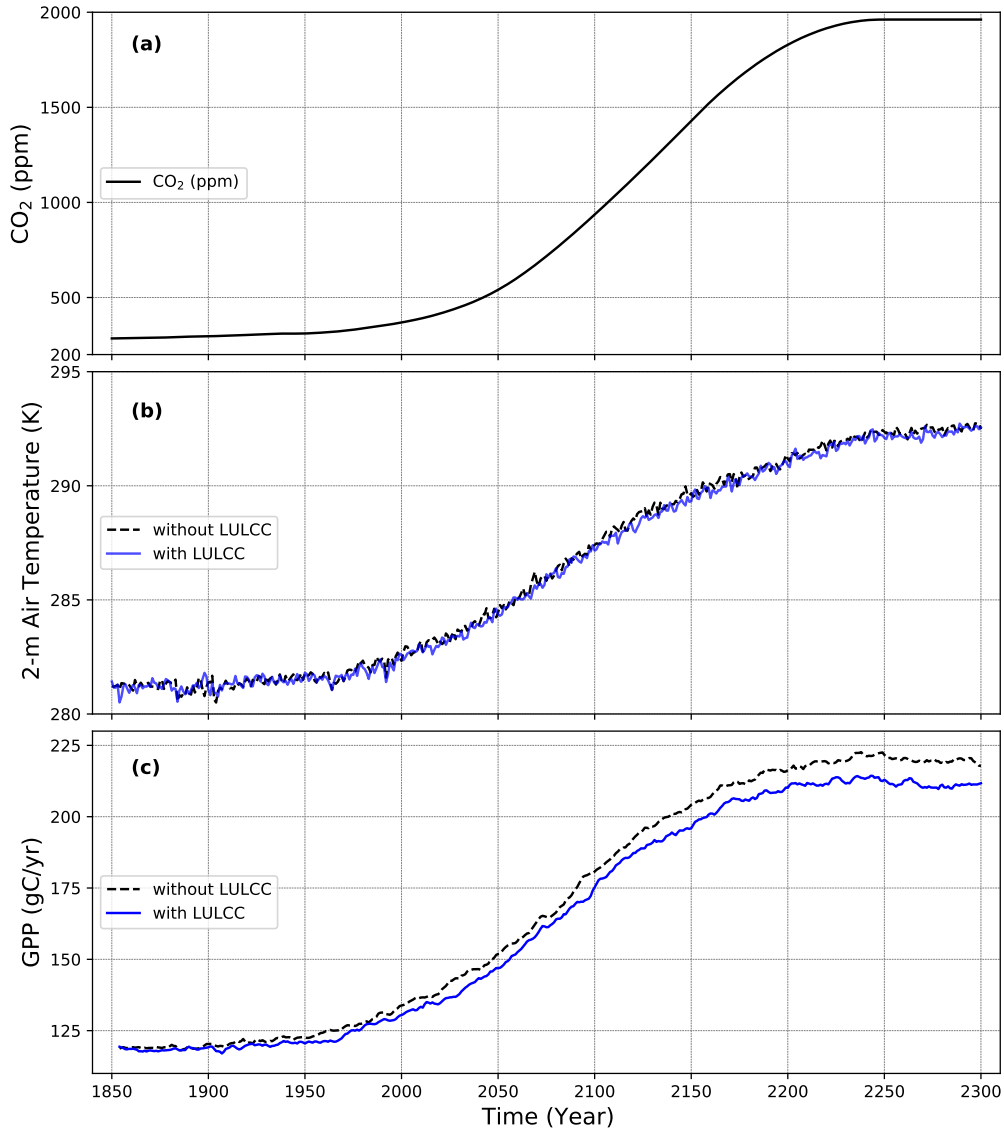


Figure 1: The (a) prescribed trajectory for atmospheric carbon dioxide (CO₂) forcing, (b) 5-year running mean of annual 2 m air temperature, and (c) 5-year running mean of total annual gross primary production (GPP) for the historical, RCP 8.5 and ECP 8.5 simulations.

negative) extreme in GPP is defined as anomalies in GPP that are greater (or less) than a selected percentile-based threshold of GPP anomalies. The thresholds were computed by selecting 1st and 99th percentile anomalies in GPP, calculated at every land grid cell for each consecutive 25 years from the year 1850 through 2300. The GPP extreme events are then defined as values of GPP anomalies above q (positive extremes) or below $-q$ (negative extremes). The schematic Figure 2 illustrates the steps to compute GPP extremes.

Extremes in GPP could also be categorized as isolated vs temporally continuous extreme events. The isolated and temporally continuous extremes in GPP are analogous to hot days and heatwaves. Extreme events in GPP that are continuous in time represent a significant cumulative impact on carbon uptake. Akin to the definition of temporally continuous heatwaves by *Baldwin et al.* (2019), we define a temporally continuous extreme (TCE) event (Figure S1) in GPP as (a) three or longer months (equal to a season length) of GPP extreme anomaly occurring consecutively, (b) and are considered as single continuous event through any gaps of two months or shorter in duration (assuming that ecological recovery is unlikely in less than a season) beyond three months. A GPP TCE event that occur after a season, i.e., three months or more, is considered a separated TCE. Section 3.2 illustrates the method for attribution of GPP TCEs to individual and compound effects of climate drivers.

3.1 Identification and Detection of GPP Extreme Events

The time series of GPP at any grid cell consists of a trend, seasonality, and anomalies (Figure 2) components. We used singular spectrum analysis (SSA), a non-parametric spectral estimation method based on embedding a time series in vector space (*Golyandina et al.*, 2001), to extract signals with specific frequencies. The trend in GPP at any grid cell captures long term change in mean GPP, which is influenced by long term changes in climate drivers, atmospheric CO₂ concentration, and LULCC. Since El Niño-Southern Oscillation (ENSO), and to a lesser extent other large-scale drivers of climate variability, enhance the variability in terrestrial photosynthesis, the nonlinear trend at each grid cell was calculated by adding all the frequencies of 10 years and longer. Hence, carbon cycle extremes in our study include the GPP anomalies induced by ENSO which is one of the largest modes of climate variability and peaks about every three to seven years (*Chylek et al.*, 2018) and exerts strong regional effects on the terrestrial carbon cycle (*Poveda*

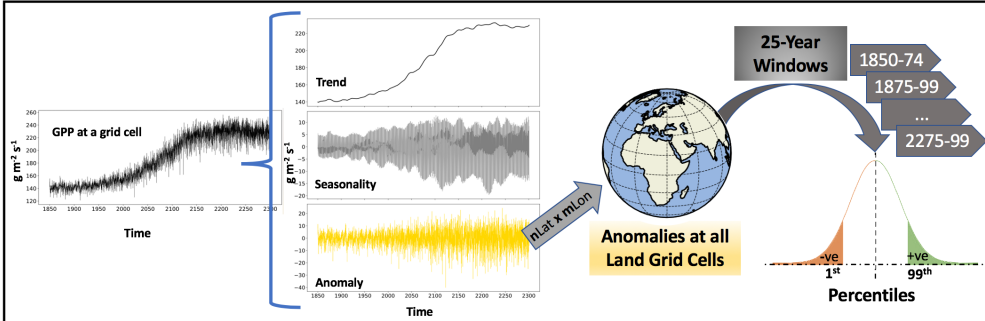


Figure 2: Schematic diagram for calculating thresholds in gross primary production (GPP). The anomalies are calculated at every grid cell by subtracting the nonlinear trend and modulated annual cycle from the GPP time series. The anomalies of every land grid cell ($nLat \times nLon$) for consecutive 25 year time windows were chosen to calculate probability distribution function of GPP anomalies. The 1st and 99th percentile values represent the global GPP threshold values for negative and positive extremes in GPP.

et al., 2001). The seasonality in GPP follows a periodic cycle of 12 months. The conventional way to compute the annual cycle is to determine the mean climatology over a period, however, the climatology does not reflect the intrinsic nonlinearity of the climate-carbon feedback, especially under external forcing (Wu et al., 2008) because of the increased modulation of the annual cycle in GPP under business-as-usual rising CO₂ emissions. We calculated the modulated annual cycle, which allows the annual cycle to change from year to year and consists of signals with a frequency of 12 months and its harmonics. The anomalies at each grid cell were calculated by subtracting the trend and modulated annual cycle from the GPP time series (Figure 2). Hence, GPP anomalies comprised of the high-frequency signals (<12 months) and the interannual variability (>12 months and <10 years). We examined the probability distribution function (PDF) of GPP anomalies for all land grid cells for every 25-year time window from 1850 through 2300. While the left tail of the PDF of GPP anomalies represents large losses in carbon uptake, the right tail portrays large gains in carbon uptake. We chose the 1st and 99th percentile of all GPP anomalies as thresholds in the 25-year time windows to identify large losses and gains in carbon uptake.

The percentile-based thresholds (1st and 99th) for every 25-year time window yield the negative ($Th-$) and positive ($Th+$) threshold trajectories of GPP anomalies. The

extreme anomalies in GPP range from 425 GgC/month for the period 1850–74 to 840 GgC/month for 2275–99, as shown in Figure 3. Since GPP anomalies are a subset of GPP, increasing CO₂ fertilization, water use efficiency, and lengthening of growing season lead to increases in GPP (Figure 1(c)) and the thresholds of GPP anomalies. The simulations *with* and *without LULCC*, show higher magnitudes of $Th-$ than $Th+$, indicating that negative anomalies in GPP are stronger than positive for the same percentile. Also, the values of the thresholds for simulation *with LULCC* were higher than *without LULCC*. To enable the comparison of simulations *with* and *without LULCC*, we selected one threshold trajectory, *without LULCC TH+ (q)*, to apply for calculations of all positive and negative extremes in the current study. Thus, the positive GPP extremes are defined as GPP anomalies greater than q and negative GPP extremes are the GPP anomalies less than $-q$ for both simulations, *with* and *without LULCC*.

Integral of negative (or positive) GPP extremes over land grid cells represents the total global loss (or gain) in carbon uptake per month. The time series of frequency and extent (area) under GPP extremes was computed by integrating the count and area of grid cells under GPP extremes.

3.2 Attribution to Climate Drivers

Human activities, through fossil fuel emissions and land cover changes, modify the climate and climate-carbon feedbacks. To attribute significant changes in carbon uptake and GPP to climate drivers, we computed linear regression of temporally continuous GPP extremes with anomalies in atmospheric precipitation (*Prcp*, composed of atmospheric rain and snow), precipitation minus evapotranspiration (*P-ET*), soil moisture (*Soilmoist*, up to 1-m depth), monthly maximum daily temperature (*T_{max}*), monthly minimum daily temperature (*T_{min}*), monthly mean daily temperature (*T_{sa}*), and fire (*Fire*, total column level carbon loss due to fire) (Table 1).

The impact of climate drivers on GPP often has a lagged response because the terrestrial ecosystem has ingrained plasticity to buffer and push back effects of climate change (Zhang *et al.*, 2014). The controls of different climate drivers on GPP and its extremes is also dependent on location, timing, soil type and moisture, and vulnerability of land cover type (Frank *et al.*, 2015). Therefore, at every location of GPP TCEs, we used linear regression to compute the correlation of TCEs with the cumulative lagged response

Table 1: Climate Drivers Considered for Attribution to GPP Extremes

Symbol	Units	Description
P_{rcp}	mm s^{-1}	Atmospheric rain + snow
$P-ET$	mm s^{-1}	Precipitation minus Evapotranspiration
$Soilmoist$	mm	Soil moisture in top 1-m depth
T_{\max}	K	Monthly maximum daily temperature
T_{sa}	K	Monthly mean daily temperature
T_{\min}	K	Monthly minimum daily temperature
$Fire$	$\text{gC m}^{-2} \text{s}^{-1}$	Total column level carbon loss due to fire

of anomalies of every climate driver at time-lags of 0 to 12 months, for every 25 year time window from 1850 to 2300. However, lagged responses beyond four months were insignificant and thus we only report on one, two, and three lags. Anomalies from past months were included in the computation of lagged correlations. For instance, to compute a climate-carbon lag response of 3 months, the GPP extreme anomalies at month t were correlated with the average of climate driver anomalies at $t-3$, $t-2$, and $t-1$ months. We also investigated the GPP TCEs driven by triggers (climate drivers during onset of TCEs) and persistent climate drivers (considering entire duration of TCEs). We identified the most dominant climate driver at any grid cell under simulations *with* and *without LULCC*, as the climate driver with the highest absolute correlation coefficient (significance value, $p < 0.05$). The percent global distributions of dominant drivers for every time window were computed to inspect the changing patterns of dominant drivers at various lags and over time.

A GPP TCE event could be driven by one or a combination of climate drivers. The study of compound events consisting of multiple different climate drivers leading to a GPP extreme improves our understanding of interactive effects of climate drivers (Zscheischler *et al.*, 2018). While the climate extremes and carbon extremes often do not occur concurrently, the compound effects of climate drivers that are not climate extremes can nevertheless impact the carbon cycle (Pan *et al.*, 2019). We studied the compound effects of water (P_{rcp} , $P-ET$, and $Soilmoist$)-, temperature (T_{\max} , T_{sa} , and T_{\min})- and fire ($Fire$)-driven TCEs in GPP.

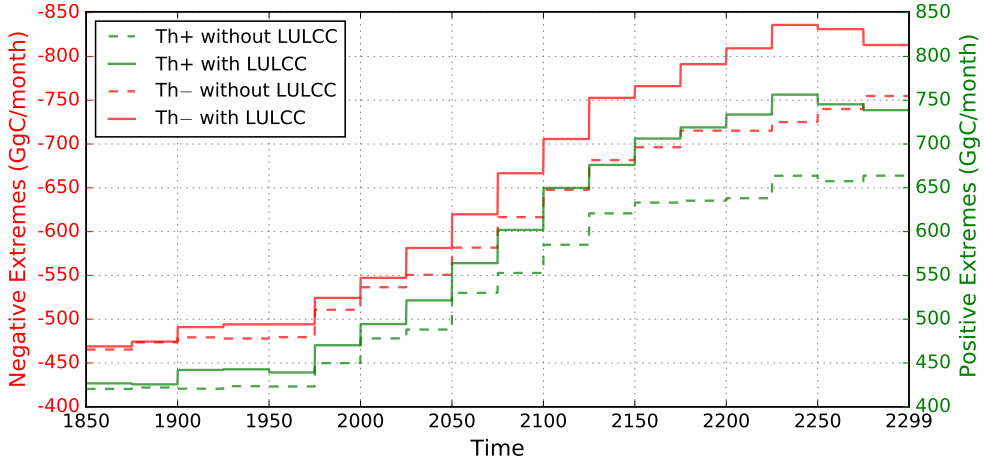


Figure 3: Thresholds of GPP extreme events *with* and *without LULCC* from 1850–2299.

The figure shows increasing thresholds of negative and positive GPP extreme events based on 1st and 99th percentile, respectively. The percentiles are calculated for global GPP anomalies for every time window (of 25 years) from 1850–2299. The red color represents negative thresholds or $Th-$ and green represents $Th+$. The solid and dashed lines represent the simulations *with* and *without LULCC* respectively.

4 Results

4.1 Detection and Identification of GPP Extremes

The 1st and 99th percentiles of the PDF of GPP anomalies for all land grid cells in 25-year time windows were used to compute the threshold trajectories for *with* and *without LULCC* simulations. Figure 3 shows trajectories of positive and negative GPP extremes for simulations *with* and *without LULCC*. The rising atmospheric CO₂ concentrations and increasing CO₂ fertilization, water use efficiency and lengthening of growing seasons (Bonan, 2015; Lawrence *et al.*, 2012) lead to an increase in the global GPP and GPP anomalies. Consequently, $Th+$ and $Th-$ increased in both simulations; for the simulation *without LULCC* $Th+$ increased from 420 GgC/month during 1850–1874 to 664 GgC/month during 2275–2299; the corresponding values for $Th+$ *with LULCC* were 426 and 739 GgC/month, for $Th-$ *without LULCC* were –465 and –755 GgC/month, and for $Th-$ *with LULCC* were –469 and –813 GgC/month. The increasing magnitude of thresholds for GPP extremes over time highlights the intensification of GPP extremes

over time. For the same percentile, the magnitude of negative thresholds were larger compared to positive thresholds. Hence, negative anomalies in GPP or losses in carbon uptake were much larger than gains in carbon uptake, primarily due to negative impact of increasing anthropogenic CO₂ and LULCC on carbon cycle anomalies. Higher thresholds for the simulation *with LULCC* despite lower GPP (Figure 1(c)) compared to the simulation *without LULCC*, highlights that increasing magnitude of GPP anomalies were likely due to LULCC and wood harvest. Higher anomalies GPP is potentially due to large reductions in the area of tree PFTs of primary vegetation (forests) in the RCP 8.5 LULCC scenario, -3.5×10^6 km² from 1850 to 2100. The decrease in primary vegetation is associated with large increases in crop and grass areas, leading to a reduction of ecosystem carbon of -49 PgC from 1850 to 2100. The global wood harvest carbon flux increased to 4.2 PgC year⁻¹ (Lawrence *et al.*, 2012) in the year 2100, and then was kept at a constant harvest rate from 2100 to 2300. The legacy effects of human land cover change and continued wood harvest becomes more visible beyond 2100 when the difference in annual GPP of both simulations widens (Figure 1(c)). As a result of enhanced variability in GPP *with LULCC*, we saw a larger magnitude of negative and positive thresholds for the simulation *with LULCC* (Figure 3).

The global time series of the intensity of losses and gains in carbon uptake, calculated by integrating negative and positive extremes in GPP, are shown in Figures 4(a) and 4(b) for simulations *without* and *with LULCC*, respectively. Compared to the simulation *without LULCC*, the total additional loss of global carbon uptake due to LULCC was -46.53 PgC for period 1850–2100 and -141.76 PgC for 2101–2300. The respective difference in total global GPP (*with LULCC* minus *without LULCC*) was -676 PgC for 1850–2100 and -1416 PgC for 2101–2300; and relative to the total global GPP, the additional losses in total carbon uptake due to LULCC increased from 6.9% (1850–2100) to 10% (2100–2300). Hence, LULCC impacts global carbon cycle by reducing the total global GPP and increasing losses in carbon uptake during GPP extremes. The rates of increase in the intensity of positive extremes in GPP for the simulation *without LULCC* were 529 and 377 MgC/month for the periods 1850–2100 and 2101–2299, respectively, and for the simulation *with LULCC* were 863 and 692 MgC/month, respectively. The corresponding rates of increase in the intensity of negative extremes in GPP for the simulation *without LULCC* were -647 and -680 MgC/month, respectively, and for the simulation *with LULCC* were -1092 and -866 MgC/month, respectively. The changes in

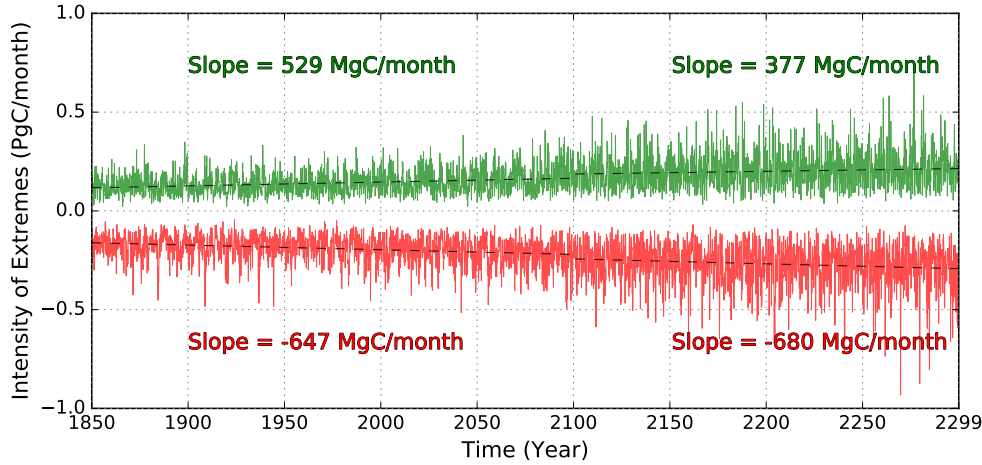
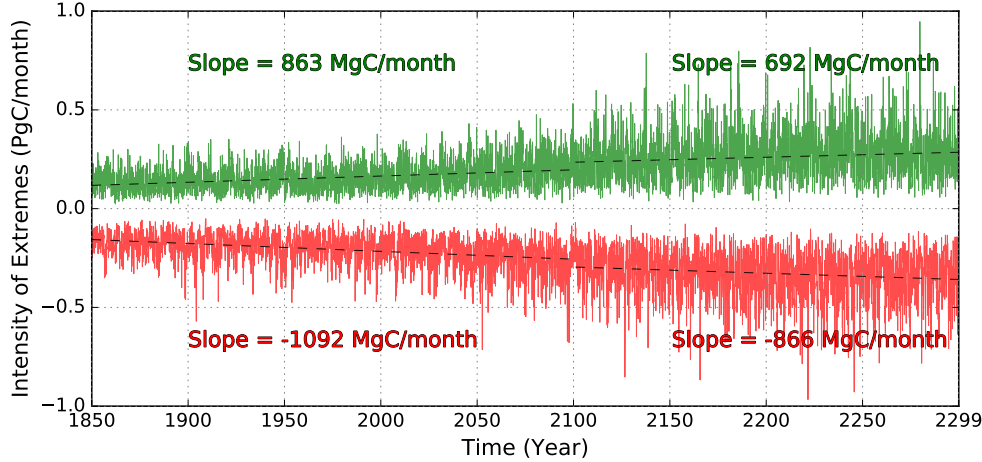
(a) Intensity of Global extremes *without LULCC* from 1850–2299(b) Intensity of Global extremes *with LULCC* from 1850–2299

Figure 4: Monthly time series of intensity of global GPP extreme events for the simulation *without LULCC* (a) and *with LULCC* (b) from 1850–2299. The positive GPP extremes, GPP anomalies $> q$, are represented in green color and the negative extremes, GPP anomalies $< -q$, are shown in red color. The rate of increase of positive GPP extremes *without LULCC* are 529 MgC/month from 1850–2099 and 377 MgC/month from 2100–2299 (a). The corresponding rates for the growth of negative extremes are -647 MgC/month and -680 MgC (a). The rate of increase of positive GPP extremes *with LULCC* are 863 MgC/month from 1850–2099 and 692 MgC/month from 2100–2299 (b). The corresponding rates for the growth of negative extremes are -1092 MgC/month and -866 MgC (b).

330 the rates of the intensity of positive extremes in GPP for the simulation *with LULCC*
331 were analogous to the simulation *without LULCC*. However, the intensity of negative ex-
332 tremes in GPP for the simulation *with LULCC* shows a decrease beyond 2100, possibly
333 due to non-increment of wood harvest rate and a constant PFT distribution at the year
334 2100 values for the period from 2100 through 2300 which decreases the relative variabil-
335 ity in GPP after 2100. The larger intensity of negative extremes in GPP for the simu-
336 lation *with LULCC* than *without LULCC* could result from increased wood harvest and
337 land conversions to agriculture, pastures, and urban areas. The rate of increase in the
338 intensity of positive extremes in GPP was higher in the simulation *with LULCC* than
339 *without LULCC* probably due to large re-growth of secondary forests in the regions of
340 the Eastern U.S., Europe, Africa, and South America (*Hurtt et al.*, 2011). In the sim-
341 ulation *with LULCC*, by the year 2100 under RCP 8.5, the LULCC transitions resulted
342 in high-density croplands in the U.S., Europe, and South East Asia; high-density pas-
343 tures in the Western U.S., Eurasia, South Africa, and Australia (*Hurtt et al.*, 2011). Pri-
344 mary forests were present in high northern latitudes and parts of Amazonia. Hence, LULCC
345 forcing coupled with CO₂ forcing under RCP 8.5 and ECP 8.5 intensified both losses and
346 gains in carbon uptake during extremes in GPP, with net losses in carbon uptake dom-
347 inating the net climate-carbon response.

348 The rate of increase of intensities of positive and negative extremes in GPP was
349 stronger for the simulation *with LULCC*, although the total GPP was less than the sim-
350 ulation *without LULCC* (Figure 1(c)). Stronger intensities of GPP extremes *with LULCC*
351 were due to the larger interannual variability (IAV) in GPP *with LULCC* compared to
352 *without LULCC* (Figure 5). LULCC alters the climate by modifying the biogeochem-
353 ical and biogeophysical processes, which further affects the carbon cycle. For example,
354 in semiarid climates, loss of vegetation cover increases the surface albedo, which increases
355 the reflected solar radiation and cools the surface climate that weakens the boundary layer,
356 reducing the probability of precipitation that creates the dry climate and reduces plant
357 productivity. Biogeochemical processes include uptake of carbon during photosynthe-
358 sis at an increased atmospheric concentration of CO₂ and loss of carbon during respi-
359 ration in a warmer climate. Biogeophysical and biogeochemical processes do not occur
360 in isolation and depend on the hydrologic cycle (*Bonan*, 2015). With increases in atmo-
361 spheric CO₂ concentration, the climate becomes warmer and increases the intensity of
362 precipitation and accompanying precipitation extremes (*Ban et al.*, 2015; *O'Gorman*,

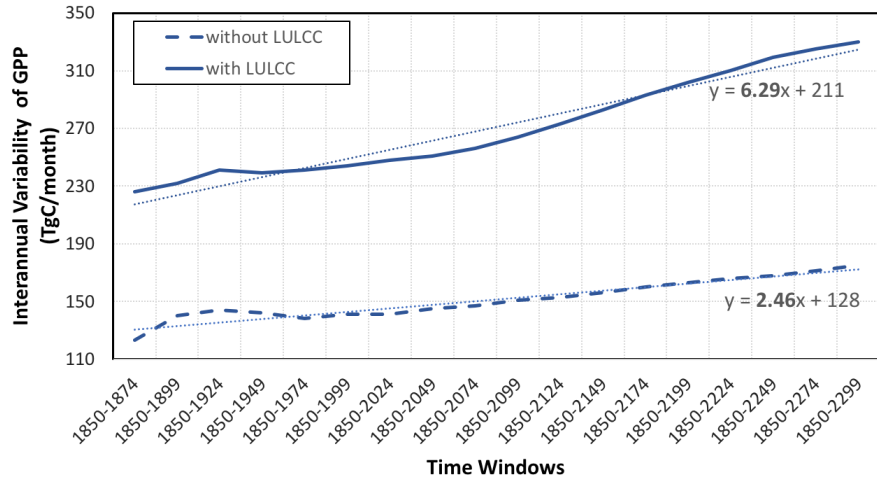


Figure 5: Global interannual variability (IAV) of GPP *with* and *without LULCC*. The unit of IAV is 10^{12} gC. The IAV is calculated from 1850 as the base year to 25 year increments, as shown on the *x*-axis. The solid line represents the IAV of GPP for *with LULCC* and dashed line represents the IAV of GPP for *without LULCC*. The linear fits represented by dotted lines show rates of increase of IAV of GPP *with LULCC*, which is higher by a factor of 2.5 compared to the simulation *without LULCC*.

2015). Clearing of land and deforestation has led to and will lead to cooling in high latitudes, warming in tropics, and uncertain changes in mid-latitudes (Lawrence *et al.*, 2016). As a result, human LULCC increases the regional heterogeneity in vegetation that alters the climate drivers (Ichii *et al.*, 2005), further increasing the global interannual variability and anomalies of GPP as well as the spatially heterogeneous distribution of GPP extremes. Therefore, the effect of both CO₂ and LULCC forcing, represented in *with LULCC*, increases the variability of biogeochemical and biogeophysical feedbacks, thus resulting in increased IAV of GPP in *with LULCC* than *without LULCC*.

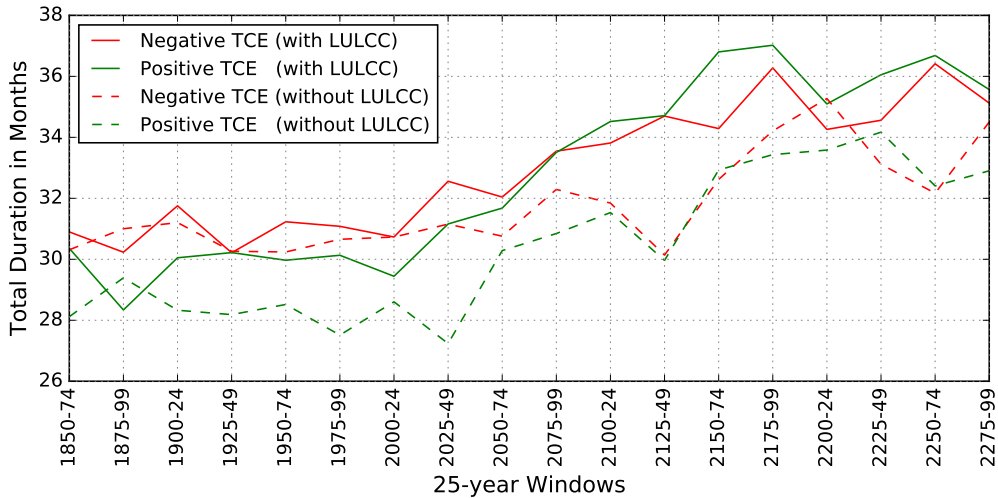
The regional atmospheric circulation and climate change lead to spatial variations in the distribution of GPP extremes and the intensities of GPP extremes. Since the definition of GPP extremes is based on the threshold trajectory of 1st percentile global anomalies of GPP for consecutive 25-year time windows in the simulation *without LULCC* (Figure 3), the total number of grid cells under positive GPP extremes were constant at around 64,000 (for every 25-year time windows) while they vary for all other scenarios. The total number of grid cells and area affected by negative extremes in GPP for the simula-

378 *with LULCC* were largest, possibly because of increased negative feedback of cli-
 379 mate variability on the carbon cycle due to the cumulative CO₂ and LULCC forcing. Rel-
 380 ative to the frequency of positive extremes in GPP for the year 1850 (*without LULCC*),
 381 the frequency of positive extremes (*with LULCC*) increased by 17% and 28% for the pe-
 382 riods 1850–2100 and 2101–2300 respectively; and the respective growth rates of nega-
 383 tive extremes (*with LULCC*) were 13% and 19%. For *with LULCC*, growth rates for the
 384 area affected by positive GPP extremes were 16% and 28%, and for negative GPP ex-
 385 tremes at 12% and 20% during 1850–2100 and 2101–2300 respectively. Higher growth
 386 rates of frequency and area-affected by positive extremes in GPP were probably due to
 387 increases in secondary forest cover; however the losses in the expected carbon uptake due
 388 to LULCC were larger than gains.

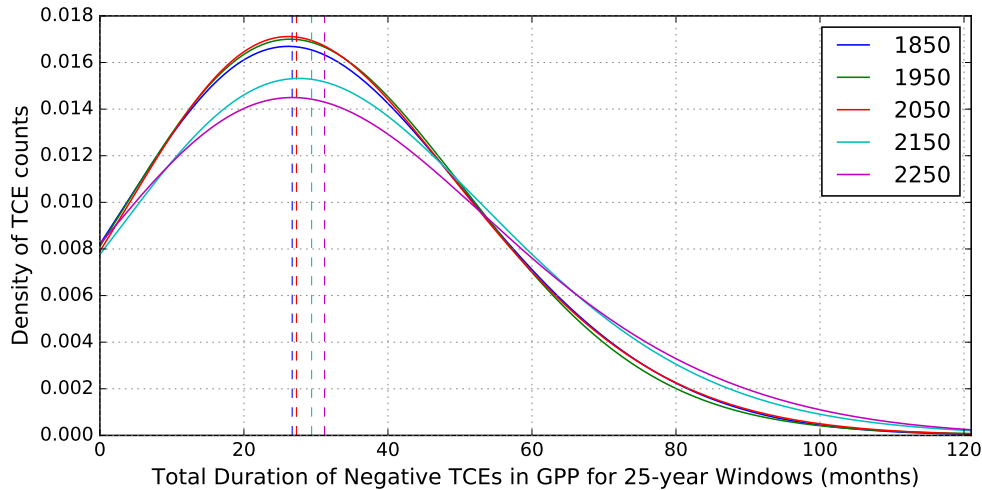
389 **4.2 Attribution to Climate Drivers**

390 The attribution of climate-driven extremes in GPP were performed for GPP TCE
 391 events, which are time-continuous GPP extremes meeting the criteria described in sec-
 392 tion 3. Variability in terrestrial carbon cycle intensified the climate-driven GPP TCEs
 393 under the combined forcing of human-induced LULCC and anthropogenic CO₂ emissions.
 394 The mean duration (Figure 6(a)) and standard deviation (Figure S2) of negative and pos-
 395 itive TCEs in GPP for the simulation *with LULCC* were greater than the simulation *with-*
 396 *out LULCC*. In addition, the duration of TCEs lengthened over time, with more long-
 397 duration TCEs and fewer short-duration TCEs as time progressed. Figure 6(b) shows
 398 the density plot of the count of negative TCEs in GPP vs. the total duration of GPP
 399 TCEs in 25-year windows for the simulation *with LULCC*. The increasing mean dura-
 400 tion of the negative TCEs in GPP in the future likely causes a larger reduction in the
 401 carbon uptake, which has significant implications for carbon storage and the carbon bud-
 402 get, and it can negate the positive feedback of increasing CO₂ fertilization under RCP 8.5
 403 and ECP 8.5 CO₂ scenarios.

404 Extremes in carbon cycle and climate extremes often do not occur simultaneously
 405 (Pan *et al.*, 2019). In this study, we first detect temporally continuous extremes (TCEs)
 406 in GPP and then attribute the climate drivers using linear regression. Pearson's corre-
 407 lation coefficients and corresponding significance values (*p*-values) were computed be-
 408 tween every climate driver and extreme anomalies in GPP during TCEs. The dominant
 409 climate driver at every land grid cell was defined by the maximum absolute correlation



(a) The mean duration of TCE events from 1850–2299



(b) Density of TCE events for a 25-year period per century

Figure 6: The mean duration of positive (shown in green) and negative (shown in red) TCEs for both the simulations, *with* (solid lines) and *without LULCC* (dashed lines), for 25-year periods (a). The probability density of counts of total number of months under a negative TCEs in 25 years or 300 months (as shown in *x*-axis) for 25-year windows starting at the years 1850, 1950, 2050, 2150 and 2250 *with LULCC* (b). The dashed vertical lines shows the shifting of mean duration of negative TCEs to right, highlighting that the TCEs are getting longer over time.

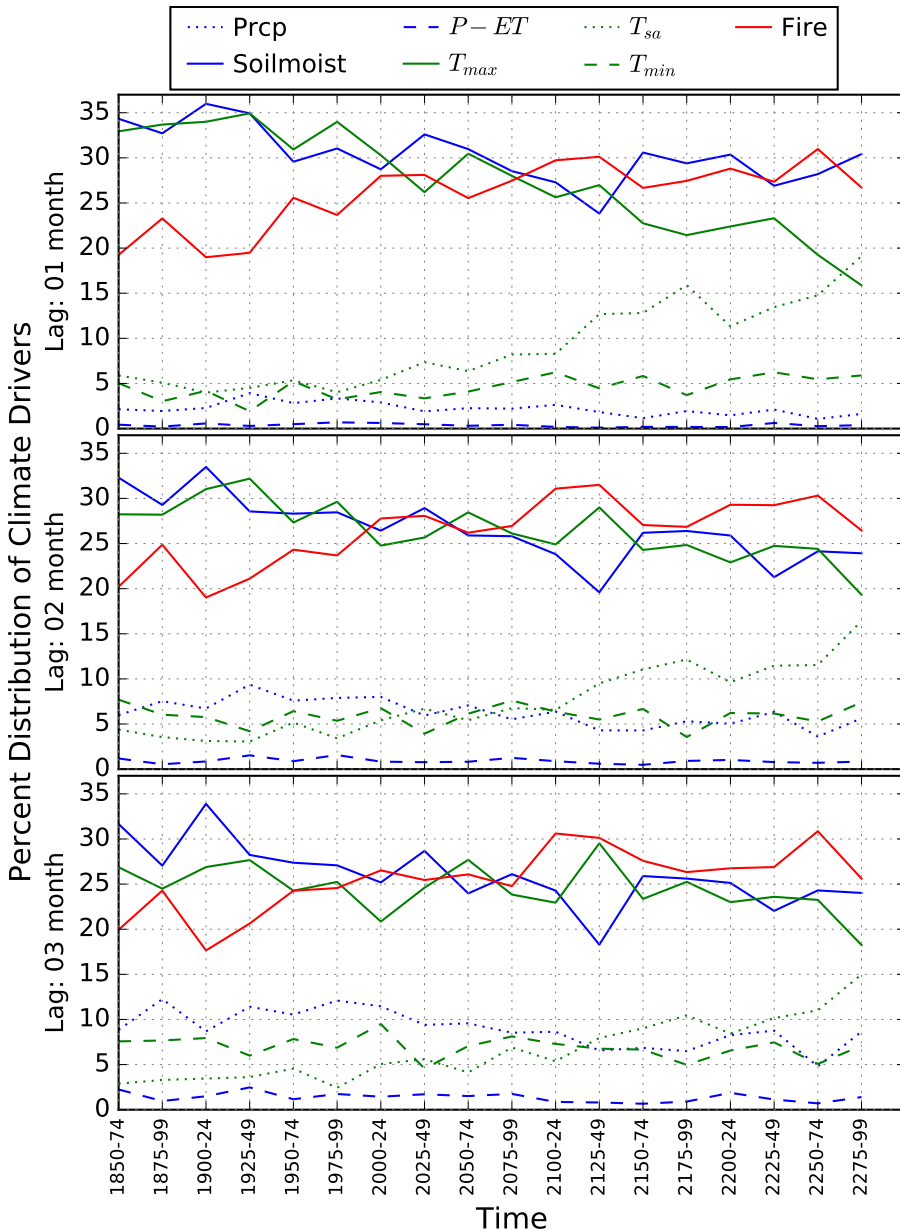


Figure 7: Percent distribution of global dominant climate drivers *with LULCC* for every time window from 1850–2299. For a particular lag month (1, 2, 3, etc.), a climate driver with highest correlation coefficient ($p < 0.05$) with carbon cycle TCEs at any grid cell is called a dominant climate driver.

410 coefficient of climate drivers ($p < 0.05$). To consider the response of the ecosystem to
411 prevailing climatic conditions, linear regressions were performed at multiple lags between
412 extreme anomalies in GPP and climate driver anomalies. Figure 7 (and Figure S3) show
413 the percent distribution of dominant climate drivers for every 25-year time window for
414 both simulations, *with LULCC* and *without LULCC*, respectively, at lags of 1, 2, and
415 3 months. The relationship of water availability (soil moisture) with TCEs in GPP was
416 globally dominant during most time windows (Figure 7). Reduction in soil moisture leads
417 to an anomalous reduction in photosynthesis (Frank *et al.*, 2015). Soil moisture is the
418 most dominant driver of negative carbon cycle extremes, highlighting a strong positive
419 correlation of plant productivity with soil moisture, as shown in Figure S4(b). Temper-
420 ature (T_{\max} and T_{sa}) and *Fire* have a negative correlation with TCEs in GPP (spatial
421 distribution shown in Figures S4(d) and S4(e)), where an anomalous increase in these
422 drivers leads to loss in carbon uptake. T_{\max} was dominant at a lag of 2 months through
423 2100, but *Fire* shows dominance at higher lags, especially beyond 2100 in the simula-
424 tion *without LULCC*. The percent count of dominant temperature drivers, T_{\max} and T_{sa} ,
425 increased over time, especially after 2100. Hence, carbon extremes driven by hot con-
426 ditions will have the largest increase in a warming climate, especially after 2100. The
427 lagged response of anomalously hot air temperatures and lack of soil moisture creates
428 hot and dry conditions suitable for fire events. Fire events driven by hot and dry con-
429 ditions increase at a higher rate at all lags in the simulation *with LULCC* than the sim-
430 ulation *without LULCC*. After 2100 in the simulation *with LULCC*, fire stands out as
431 the dominant driver at all lags, highlighting that the human-induced LULCC will make
432 ecosystems more vulnerable to fire events. The results of our study are consistent with
433 the findings of Williams *et al.* (2014) and Zscheischler *et al.* (2014), suggesting that the
434 declines in GPP with warm temperature extremes are due to dependence of GPP on soil
435 moisture, and to the strong negative correlation between soil moisture and temperature.
436 The rising temperature under global warming will create a warmer environment in the
437 future, increasing the risk associated with heatwaves and their impacts on the ecosys-
438 tem. A decline in precipitation and soil moisture compounded with warm temperature
439 may cause an unprecedented increase in loss of carbon uptake and potentially reduce the
440 terrestrial carbon sink.

441 The combined effect of climate drivers often has a larger impact on extremes in car-
442 bon cycle than the simple addition of individual climate drivers (Zscheischler *et al.*, 2018, 2014;

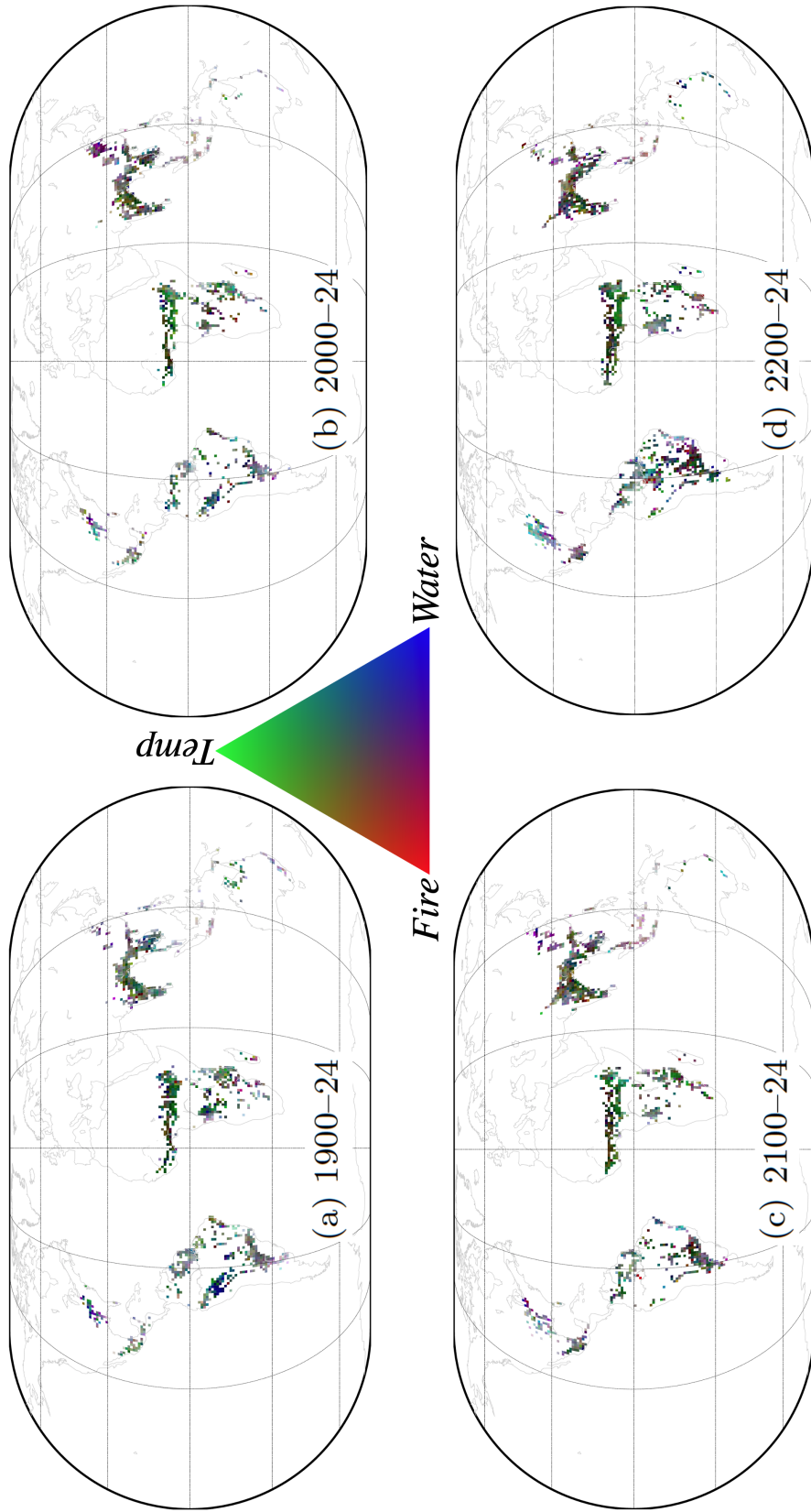


Figure 8: Spatial distribution of climate drivers causing negative TCEs in GPP for *with LULCC* for four 25-year time windows, (a) 1900–24, (b) 2000–24, (c) 2100–24, and (d) 2200–24. The climate drivers are pooled in three colors, red, green, and blue. Red (*Fire*) is for loss of carbon due to fire, green (*Temp*) represents monthly maximum, mean, and minimum daily temperatures (T_{\max} , T_{sa} , T_{\min} respectively), Blue (*Water*) includes monthly means of soil moisture, precipitation and $P-E$ (precipitation minus evapotranspiration). The results shown here are at 1 month lag.

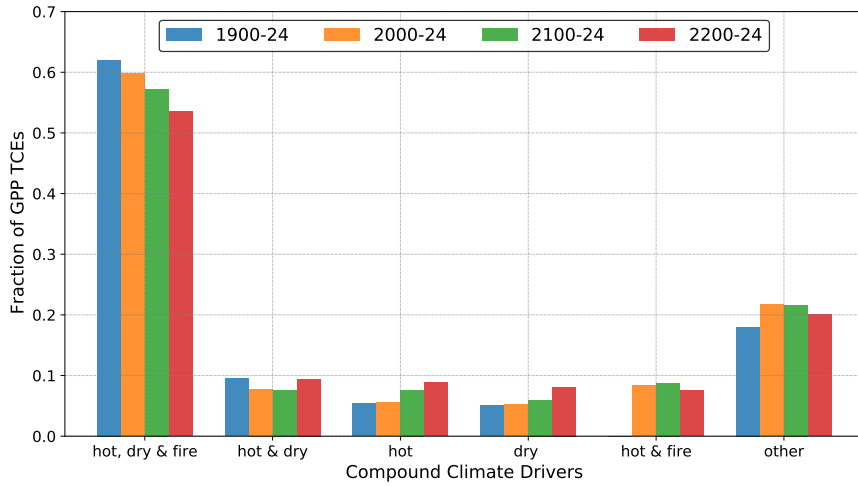


Figure 9: Attribution of temporally continuous extreme events in GPP to compound effect of climate drivers for *with LULCC* at lag of 1 month for 25-year time windows, (a) 1900–24, (b) 2000–24, (c) 2100–24, and (d) 2200–24. The fractions are mutually exclusive, i.e., events driven by *hot and dry* climate is not counted in either *hot* or *dry* climate driven events. Any location could be affected by one or compound climatic conditions. For example, a carbon cycle extreme could be driven by any combination of hot or cold, dry or wet, and with or without fire. We only show the combination of driving climate drivers that have total fraction of more than 0.05.

443 *Frank et al., 2015; Flach et al., 2020*). To capture the compound effect of climate drivers
444 (Table 1) on GPP TCE events, the climate drivers were grouped under fire, tempera-
445 ture, and water-driven extremes (Section 3.2). Figures 8 and S5 show the spatial distri-
446 bution of climate drivers at a lag of one month for simulations *with* and *without LULCC*,
447 respectively. We observed an increase in the number of TCEs in GPP and changes in
448 the spatial distribution of GPP TCEs and climate drivers for time periods 1900–24, 2000–
449 24, 2100–24, and 2200–24 in the simulation *with LULCC* (Figure 8). Most locations ex-
450 perienced TCE events due to the combined effects of all the climate drivers.

451 We computed all combinations of water (dry or wet), temperature (hot or cold),
452 and fire-driven climatic conditions that cause GPP TCEs. For brevity, we report results
453 for one 25-year time window one per century. The fractions (larger than 0.05) of total
454 negative TCEs in GPP driven by mutually exclusive climate conditions are shown in Fig-
455 ure 9. More than half of the total TCEs in GPP occurred when the environmental con-
456 ditions are hot and dry, resulting in fire events and account for large reductions in GPP
457 (Figure 8 and 9). Similar to other studies (*Zscheischler et al., 2014; Frank et al., 2015*),
458 a stronger correlation between warm and dry climate has a substantial impact on the
459 terrestrial carbon cycle. The increased fraction of TCEs attributed to hot climate over
460 time is possibly due to combined attribution of T_{\max} and T_{sa} , as shown in Figure 7. Fig-
461 ure S6 represents the total fraction of TCEs in GPP driven by mutually inclusive climatic
462 conditions. As global warming increases the temperature of the planet, ecosystems will
463 become more vulnerable to the hot and dry climate and at increasing risk of fire events
464 (Figure 9).

465 Here we highlight the temporal changes in the distribution of carbon cycle extremes
466 and their climate drivers for the simulation *with LULCC*. East Asia experiences a large
467 number of TCEs during the 21st century (Figure 8) driven by dry climate and fire, which
468 however declines in the 22nd due to an increase in precipitation and available soil mois-
469 ture. The Savannas near Congo in Africa display an increased vulnerability of vegeta-
470 tion to fire and hot temperatures. The impact of LULCC in Savannas is prominent af-
471 ter 2100 (Figures S5(d) and 8(d)) when the pattern of dominant drivers change from temperature-
472 driven (green color) to a compound effect of increase in dry, hot, and fire conditions (gray
473 color). The contiguous United States (CONUS) experiences more GPP TCEs, especially
474 in the 23rd century (Figure 8(d)), driven by hot temperature and water limitation (high-
475 lighted in cyan color). Indonesia and its neighboring islands show increasing GPP TCEs

476 attributed to a combination of hot temperatures and fire. The number of negative TCEs
 477 in South America are approximately the same for periods in Figures 8(a), 8(b) and 8(c)
 478 except for the period 2200–24 (Figure 8(d)) when the extremes show a large increase. Dur-
 479 ing 2200–24, South America shows a drastic increase in negative TCEs that is attributed
 480 primarily to dry, hot, and fire conditions (represented by gray color). Africa experiences
 481 an increase in the number of GPP TCEs attributed to hot climate, and, in the far fu-
 482 ture (2101–2300), witnesses an increased frequency of fire events. Australia’s east coast
 483 also exhibits an increase in GPP TCEs because of water limitation, dry climate, and they
 484 are accompanied by fires in the far future. The South and Southeast Asia (composed of
 485 India, Myanmar, Thailand, and Cambodia) experiences an increase in TCEs in GPP over
 486 time. These Asian regions where primary forest were converted to cropland (*Hurtt et al.*,
 487 2011), saw an increase in fire-driven extreme events in GPP, highlighting a rising vul-
 488 nerability to fire events due to LULCC.

489 5 Discussion

490 5.1 Regional Analysis of Climate Change Impact on Climate Drivers 491 and Negative Carbon Cycle Extremes

492 Most climate models show an increase in the interannual variability of land–atmosphere
 493 CO₂ exchange over time (*Keenan et al.*, 2012). The increasing atmospheric CO₂ con-
 494 centration influences climate through its radiative effect (i.e., Greenhouse effect) and in-
 495 directly through physiological effect (reduced plant transpiration) (*Cao et al.*, 2010). The
 496 increasing radiative effects cause changes in circulation, impacting precipitation, soil mois-
 497 ture, and global scale water cycle. Increase in precipitation and CO₂ fertilization and
 498 reduction in stomatal conductance could lead to an increase in GPP; however, droughts,
 499 heatwaves and fires curtail plant photosynthesis (*Swann et al.*, 2016). Under climate change,
 500 while most regions experience an increase in mean GPP, some regions exhibit a decline.

501 Reduction in growth rate of expected terrestrial carbon uptake below carbon emis-
 502 sions could lead to weakening of carbon sink capacity (Figure S7). Increase in total GPP
 503 and IAV in GPP over time contribute to the increase in magnitude of negative carbon
 504 cycle extremes. However, some regions experience weakening of negative carbon cycle
 505 extremes often due to decline in total GPP, and reduction in IAV of GPP and climate
 506 drivers (Figure S8). Driven by large scale circulation changes, increasing temperature

and decreasing precipitation and soil moisture in Central America (CAM) lead to forest mortality, decline in GPP and weakening of negative carbon cycle extremes. The decrease in precipitation in the Northern South American Tropics (NSA) and Central Amazon Basin (CAB) and increase in precipitation in the Southwest Amazon Basin (SAB) is due to plant physiologic response. *Langenbrunner et al.* (2019) investigated this phenomenon in the regions of the Amazon and the Andes and found that under increased atmospheric CO₂, stomatal conductance decreases, reducing water loss through transpiration, which decreases the convective activity and causes a reduction in rainfall over the Amazon Basin (CAB, NSA) and increases moisture advection by low-level westward jets towards the Andes, leading to increases in the rainfall over the Andes (SAB). Reducing variability and increasing precipitation over SAB increase available soil moisture increasing regional GPP, however with reduced IAV, resulting in weakening of negative carbon cycle extremes. Although CAB witnesses a decline in precipitation it demonstrates an increase in GPP likely due to slight reduction in soil moisture and large CO₂ fertilization effect which compensates for the reduction in soil moisture. Hence, in CAB both GPP and IAV in GPP increases over time causing strengthening of negative carbon cycle extremes. These regional patterns of changes in GPP, negative carbon cycle extremes, and climate drivers are seen across the globe. For example, the regional changes in Northern Guinea, Southern Guinea, Central Guinea and Indonesia resemble the processes in CAM, SAB, CAB and CAM, respectively. Additional feedbacks due to LULCC – as tropical forests are replaced with crops or grasslands that transpire less than forests, further reducing rainfall over the Amazon – causes hotter and drier climate with an increasing risk of fire and larger losses of carbon uptake (Figures S9 and S10).

Our robust attribution analysis based on successive time windows captures the changes in the anomalies of climate drivers and carbon cycle. During 1900–24 and 2000–24, most of the negative TCEs in GPP that occurred in SAB (Figure 8), were due to water limitation (highlighted by the blue color in the RGB maps). With increased water availability in SAB (*Langenbrunner et al.*, 2019), the effects of heat associated with temperature increases are mitigated and the number of negative carbon cycle extremes reduces. The decrease in precipitation in NSA led to a reduction in soil moisture, resulting in a hot and dry climate, thus making the vegetation prone to fire at high temperatures (the compound effect is highlighted by the gray color). The reduced GPP in NSA over time further leads to a fewer number of negative carbon cycle extremes (Figure 8). Large IAV

540 and anomalies in GPP in CAB lead to increased concentration of negative TCEs in GPP
 541 driven possibly due to combined effect of increased hot, dry, and fire events (shown in
 542 gray color).

543 5.2 Drivers and Triggers of Carbon Cycle Extremes

544 A grid cell could experience any number of extreme events of any length during suc-
 545 cessive 25 year time windows from 1850 through 2300. Our methodology helps identify
 546 long temporally continuous extremes which represent large magnitude carbon extremes
 547 and have higher significant regression coefficient. We use this methodology to identify
 548 the prevailing climatic conditions that act as triggers for an extreme and the conditions
 549 that cause an extreme to persist. We demonstrate the findings from Chaco Province in
 550 Argentina where the major plant functional type is broadleaf deciduous tree (43%).

551 Under the simulation *without LULCC* and the time period 2000–24, the total num-
 552 ber of positive TCE events in GPP were seven with a total duration of 53 months, which
 553 were greater than the total five negative TCEs in GPP with a total duration of 40 months
 554 (Table S2). The total gain in carbon uptake was 35.17 TgC, which was greater than the
 555 total loss in carbon uptake of –28.15 TgC, resulting in a net gain in carbon during TCE
 556 events. Under the simulation *with LULCC*, during the same period of 2000–24 the to-
 557 tal number of negative GPP TCEs (6 events, 57 months) were greater than positive TCEs
 558 (5 events, 35 months). Thus, the total loss in carbon uptake (–35.86 TgC) *with LULCC*
 559 was higher than the gain in carbon uptake (23.87 TgC). While this region had a net gain
 560 in carbon uptake of 7.02 TgC for the simulation *without LULCC*, and it had a net loss
 561 in carbon uptake of –11.99 TgC for the simulation *with LULCC*. The increase in neg-
 562 ative extremes in GPP with net losses in carbon uptake demonstrates the role of human-
 563 induced LULCC in negatively affecting carbon uptake capacity.

564 We performed a qualitative investigation of every negative and positive TCEs in
 565 GPP (Figure S11) using normalized time series of GPP, GPP anomalies and anomalies
 566 of major climate drivers (*Prcp*, *Soilmoist*, *T_{max}*, and *Fire*). Most positive TCEs in GPP
 567 were driven by increase in precipitation, followed by rise in soil moisture and decline in
 568 *T_{max}*. Most negative extremes in GPP were driven by decline in precipitation and ris-
 569 ing *T_{max}*, which cause high evapotranspiration and loss of soil moisture, eventually cre-

570 ating dry and hot conditions that cause fire events. Some of the negative extremes in
 571 these regions were also found to be driven by hot and dry events without fire.

572 To identify the triggers of carbon cycle extremes, we define the onset period of GPP
 573 TCEs as first-quarter of every TCE. The regression onset period of GPP TCEs and anomalies
 574 of climate drivers were computed with consideration of the lagged response of cli-
 575 mate drivers on GPP TCEs. The lagged soil moisture anomalies were highly correlated
 576 ($p < 0.01$) with entire duration of TCE events (persistence, Table S3), and the lagged
 577 precipitation anomalies were highly correlated with the onset (trigger, Table S4) of TCE
 578 events in the Chaco Province.

579 For the simulation with CO₂ only forcing (i.e. *without LULCC*) during time pe-
 580 riod 2000–24, the correlation coefficient, for the whole duration of GPP TCEs, was high-
 581 est for soil moisture anomalies at a lag of 1 month. The precipitation anomalies had high
 582 positive correlations with GPP TCEs (i.e., reduction in precipitation was correlated with
 583 a decrease in GPP) at lags of 3 and 4 months. T_{\max} and *Fire* had large negative cor-
 584 relations with GPP anomalies (i.e., increase in temperature correlates with a decrease
 585 in GPP or increase in carbon uptake loss) at a lag of 2 months. Hence, for a negative
 586 GPP TCE event, the compound effect of a decline in precipitation followed by increase
 587 in temperature caused a reduction of soil moisture, resulting in hot and dry conditions,
 588 increasing the probability of occurrence of fire and causing a long negative TCE event
 589 ($Precip > T_{\max} > Soilmoist > TCE$). For the same region under simulation *with LULCC*,
 590 the dominant trigger was T_{\max} (Table S5) followed by precipitation. Therefore, human-
 591 induced LULCC coupled with increasing CO₂ levels tends to enhance the vulnerability
 592 and loss in vegetation due to hot and non-dry climate conditions, resulting in more neg-
 593 ative extremes in GPP. The analysis illustrates the strength of our methodology in iden-
 594 tifying the evolution of carbon cycle extremes for multiple conditions and at fine reso-
 595 lution.

596 5.3 Limitations of CESM1(BGC)

597 The ILAMB benchmarking scores (*Collier et al.*, 2018) of the carbon fluxes and
 598 climate drivers indicate that CESM1(BGC) is among the best CMIP5 models (Table S1).
 599 However, the Community Land Model version 4 (CLM4), the land model used in the CESM1(BGC)
 600 (*Oleson et al.*, 2010), had some limitations which could potentially impact some of our

601 findings. The simulated GPP by CLM4 had a positive bias across the globe compared
602 to FLUXNET eddy covariance tower estimates due to lack of colimitation of GPP to canopy
603 scaling and parameterization of leaf photosynthesis kinetics (*Bonan et al.*, 2011). With
604 improvements in the model parameterizations of radiative transfer, leaf photosynthesis
605 and stomatal conductance, canopy scaling of leaf processes, inclusion of multilayer canopy
606 model, and updated maximum rate of electron transfer parameters (*Bonan et al.*, 2011, 2012b),
607 the positive bias in GPP was reduced. With inclusion of vertically resolved CN model
608 in CLM4.5 (*Koven et al.*, 2013), the positive bias in GPP was further improved and ter-
609 restrial carbon storage increased consistently with observations. In the current study fo-
610 cused on the patterns of carbon cycle extremes, the positive bias of GPP was likely cap-
611 tured by trend and removed for calculation of GPP anomalies. However, any associated
612 increase in the IAV of GPP corresponding to positive bias of GPP would increase the
613 magnitude of GPP anomalies and both negative and positive GPP extremes. Thus, there
614 is a potential to overestimate the magnitude of both negative and positive GPP extremes
615 but the relative comparison is insightful and most likely not affected by this limitation
616 of CLM4.

617 CLM4 lacks representation of dynamic crop, thus the cooling effects in irrigated
618 lands, changes in the sensible and latent heat, and soil carbon change are not well rep-
619 resented in CLM4.0 but were improved in the CLM5.0 (*Lombardozzi et al.*, 2020). The
620 simulated climate-carbon feedbacks in CLM4 assume an instantaneous response of plant
621 physiological processes to changes in temperature (*Lombardozzi et al.*, 2015). With in-
622 clusion of temperature acclimation, though the ecosystem carbon storage pool grew (mostly
623 in higher latitudes), the effect on photosynthesis of tropical regions was minimal. Since
624 most of the detected extremes in the tropical forest and other high biomass regions, the
625 lack of representation of agriculture and temperature acclimation on GPP are not ex-
626 pected to have significant effect on the analysis of extremes.

627 6 Conclusions

628 Using the fully-coupled Earth system model, CESM1(BGC), we analyzed the de-
629 velopment of extreme events in GPP and attributed those carbon cycle extremes to cli-
630 mate drivers from the year 1850 through 2300 for simulations *with* and *without LULCC*.
631 While both simulations were forced with RCP 8.5 and ECP 8.5 atmospheric CO₂ con-
632 centrations, only the simulation *with LULCC* had additional forcing from human-induced

land use and land cover change (LULCC). The changes in land cover directly modify the biogeophysical and biogeochemical feedbacks of terrestrial vegetation and indirectly through the physiological responses of vegetation on climate drivers, leading to increase in interannual variability in GPP and higher magnitude of GPP anomalies. Relative to the simulation *without LULCC*, the simulation *with LULCC* exhibited increased variability in GPP and higher intensity, duration, extent, and frequency of extremes in GPP. These characteristics were greater for negative extremes in GPP than positive extremes, implying larger than expected losses in carbon uptake than carbon gains. Although the total GPP for the simulation *with LULCC* was less than the total GPP *without LULCC*, the simulation *with LULCC* showed a sharper decline of carbon uptake of -6.9% in the near future (1850–2100) and -10% in the far future (2100–2300) with respect to total GPP *without LULCC*. The interactive effects of LULCC with the RCP 8.5 and ECP 8.5 CO₂ forcing amplify the weakening of the net carbon uptake, and a reduction of land carbon sink capacity, which could greatly affect the global carbon budget.

Increasing atmospheric CO₂ concentrations drive growth in vegetation photosynthesis or GPP due to carbon fertilization, and reduction in stomatal conductance. Therefore, most places exhibited increased GPP and higher interannual variability in GPP. Due to circulation changes, a few regions witness a decrease in precipitation, creating a drier climate that when supplemented with warmer temperatures lead to decline in GPP, such as the regions of the eastern Amazon and Central America. Reducing magnitudes of GPP over time and analogous decreases in the interannual variability of GPP produce weakening of negative carbon cycle or GPP extremes in the Amazon. Moreover, the weakening of other negative carbon cycle extremes could be a result of less variable and benign climatic conditions for vegetation productivity, as seen around the Andes. Hence, it is imperative to inspect trends in GPP and negative carbon cycle extremes simultaneously to understand the nature of changes in extremes and their implications at regional scales.

We found that the duration of GPP TCEs increased with higher CO₂ concentration, i.e., a location experienced GPP TCEs with increasing duration over time. The duration and impact of negative TCEs in GPP are enhanced when human-induced LULCC was considered, resulting in increased loss in carbon uptake. We illustrated this with the case study of the Chaco Province in Argentina that had a net gain in carbon uptake (7.02 TgC)

665 during 2000–24 in the simulation *without LULCC* and while a net loss in carbon uptake
666 (-11.99 TgC) in the simulation *with LULCC*.

667 The single most dominant climate driver was soil moisture that had highest cor-
668 relations with GPP extremes ($p < 0.05$) and the correlations were mostly positive, in-
669 dicating that anomalous decrease in soil moisture or drier climate conditions cause anom-
670 lous reductions in GPP. Other major individual drivers were hot temperatures and fire.
671 Fire was a dominant climate driver, especially after 2100 in the simulation *with LULCC*,
672 highlighting the increased vulnerability of ecosystems to fire events due to the impact
673 of human activities on ecosystems. We also found that the decline in precipitation trig-
674 gers a negative carbon cycle TCE event, but the reduction in soil moisture or water lim-
675 itation was the dominant driver for those negative carbon cycle TCE events to persist.
676 The compound effects of climate drivers were also analyzed, and an increasing number
677 of regions under carbon cycle extremes were attributed to hot and dry conditions. The
678 largest fraction of negative carbon cycle extremes were driven by the compound effects
679 of hot, dry, and fire events. Warmer conditions under climate change increases the risk
680 of occurrence of fire events and their impacts on the carbon cycle and extremes of the
681 future.

682 This study presents a detailed analysis of detection and identification of carbon cy-
683 cle extreme events, how these extremes evolve from 1850 through 2300, and how human-
684 induced LULCC alters them using a fully coupled Earth system model forced with the
685 RCP 8.5 and ECP 8.5 CO₂ concentration scenarios. It also attributes the climate drivers
686 of such extremes in carbon cycle for the periods 1850–2100 and 2100–2300, and analyzes
687 the changing patterns and dominance of climate drivers, under *with* and *without LULCC*
688 scenarios. Study provides new insights into the contribution of human activities in al-
689 tering carbon cycle extremes and the vulnerability of terrestrial vegetation and associ-
690 ated ecosystem services that could present increasing risks to human lives, wildlife, and
691 food security.

Acknowledgments

We thank the Community Earth System Model (CESM) Biogeochemistry Working Group (BGCWG) for performing the CESM1(BGC) simulations analyzed in this study. This research was supported by the Reducing Uncertainties in Biogeochemical Interactions through Synthesis and Computation (RUBISCO) Science Focus Area, which is sponsored by the Regional and Global Model Analysis (RGMA) activity of the Earth & Environmental Systems Modeling (EESM) Program in the Earth and Environmental Systems Sciences Division (EESSD) of the Office of Biological and Environmental Research (BER) in the US Department of Energy Office of Science. This research used resources of the Compute and Data Environment for Science (CADES) at the Oak Ridge National Laboratory, which is managed by UT-Battelle, LLC, for the US Department of Energy under Contract No. DE-AC05-00OR22725.

Open Research**Data Availability Statement**

The CESM1(BGC) model output used for detection and attribution of carbon cycle extremes in the study are available at <https://doi.org/10.5281/zenodo.5548153>. Data analysis was performed in Python, and all analysis codes are publicly available on GitHub at https://github.com/sharma-bharat/Codes_Carbon_Extremes_2300 and archived at <https://doi.org/10.5281/zenodo.6147120>.

711 **References**

- 712 Baldwin, J. W., J. B. Deyssy, G. A. Vecchi, and M. Oppenheimer (2019), Temporally
 713 compound heat wave events and global warming: An emerging hazard, *Earth's
 714 Future*, 7(4), 411–427, doi:10.1029/2018EF000989.
- 715 Ban, N., J. Schmidli, and C. Schär (2015), Heavy precipitation in a changing cli-
 716 mate: Does short-term summer precipitation increase faster?, *Geophysical Re-
 717 search Letters*, 42(4), 1165–1172, doi:10.1002/2014GL062588.
- 718 Bonan, G. (2015), *Ecological Climatology: Concepts and Applications*, 3 ed., Cam-
 719 bridge University Press, doi:10.1017/CBO9781107339200.
- 720 Bonan, G. B., P. J. Lawrence, K. W. Oleson, S. Levis, M. Jung, M. Reichstein,
 721 D. M. Lawrence, and S. C. Swenson (2011), Improving canopy processes in
 722 the community land model version 4 (clm4) using global flux fields empirically
 723 inferred from fluxnet data, *Journal of Geophysical Research: Biogeosciences*,
 724 116(G2), doi:10.1029/2010JG001593.
- 725 Bonan, G. B., R. S. DeFries, M. T. Coe, and D. S. Ojima (2012a), Land use and
 726 climate, in *Land change science. Remote Sensing and Digital Image Processing*,
 727 vol. 6, pp. 301–314, Springer, doi:10.1007/978-1-4020-2562-4_17.
- 728 Bonan, G. B., K. W. Oleson, R. A. Fisher, G. Lasslop, and M. Reichstein (2012b),
 729 Reconciling leaf physiological traits and canopy flux data: Use of the try and
 730 fluxnet databases in the community land model version 4, *Journal of Geophysical
 731 Research: Biogeosciences*, 117(G2), doi:10.1029/2011JG001913.
- 732 Cao, L., G. Bala, K. Caldeira, R. Nemani, and G. Ban-Weiss (2010), Importance of
 733 carbon dioxide physiological forcing to future climate change, *Proceedings of the
 734 National Academy of Sciences*, 107(21), 9513–9518, doi:10.1073/pnas.0913000107.
- 735 Chylek, P., P. Tans, J. Christy, and M. K. Dubey (2018), The carbon cycle response
 736 to two el nino types: an observational study, *Environmental Research Letters*,
 737 13(2), 024,001, doi:10.1088/1748-9326/aa9c5b.
- 738 Collier, N., F. M. Hoffman, D. M. Lawrence, G. Keppel-Aleks, C. D. Koven, W. J.
 739 Riley, M. Mu, and J. T. Randerson (2018), The international land model bench-
 740 marking (ilamb) system: Design, theory, and implementation, *Journal of Advances
 741 in Modeling Earth Systems*, 10(11), 2731–2754, doi:10.1029/2018MS001354.
- 742 Flach, M., A. Brenning, F. Gans, M. Reichstein, S. Sippel, and M. D. Mahecha
 743 (2020), Vegetation modulates the impact of climate extremes on gross primary

- 744 production, *Biogeosciences Discussions*, 2020, 1–20, doi:10.5194/bg-2020-80.
- 745 Frank, D., M. Reichstein, M. Bahn, K. Thonicke, D. Frank, M. D. Mahecha,
746 P. Smith, M. van der Velde, S. Vicca, F. Babst, C. Beer, N. Buchmann, J. G.
747 Canadell, P. Ciais, W. Cramer, A. Ibrom, F. Miglietta, B. Poulter, A. Rammig,
748 S. I. Seneviratne, A. Walz, M. Wattenbach, M. A. Zavala, and J. Zscheischler
749 (2015), Effects of climate extremes on the terrestrial carbon cycle: concepts, pro-
750 cesses and potential future impacts, *Global Change Biology*, 21(8), 2861–2880,
751 doi:10.1111/gcb.12916.
- 752 Golyandina, N., V. Nekrutkin, and A. A. Zhigljavsky (2001), *Analysis of Time*
753 *Series Structure: SSA and Related Techniques*, 1 ed., 320 pp., Chapman and
754 Hall/CRC, doi:10.1201/9781420035841.
- 755 Hoffman, F. M., J. T. Randerson, V. K. Arora, Q. Bao, P. Cadule, D. Ji, C. D.
756 Jones, M. Kawamiya, S. Khatiwala, K. Lindsay, A. Obata, E. Shevliakova,
757 K. D. Six, J. F. Tjiputra, E. M. Volodin, and T. Wu (2014), Causes and impli-
758 cations of persistent atmospheric carbon dioxide biases in earth system mod-
759 els, *Journal of Geophysical Research: Biogeosciences*, 119(2), 141–162, doi:
760 10.1002/2013JG002381.
- 761 Hubau, W., S. L. Lewis, O. L. Phillips, K. Affum-Baffoe, H. Beeckman, A. Cuní-
762 Sanchez, A. K. Daniels, C. E. Ewango, S. Fauset, J. M. Mukinzi, et al. (2020),
763 Asynchronous carbon sink saturation in African and Amazonian tropical forests,
764 *Nature*, 579(7797), 80–87, doi:10.1038/s41586-020-2035-0.
- 765 Hurt, G. C., L. P. Chini, S. Frolking, R. A. Betts, J. Feddema, G. Fischer, J. P.
766 Fisk, K. Hibbard, R. A. Houghton, A. Janetos, C. D. Jones, G. Kindermann,
767 T. Kinoshita, K. Klein Goldewijk, K. Riahi, E. Shevliakova, S. Smith, E. Stehfest,
768 A. Thomson, P. Thornton, D. P. van Vuuren, and Y. P. Wang (2011), Harmoniza-
769 tion of land-use scenarios for the period 1500–2100: 600 years of global gridded
770 annual land-use transitions, wood harvest, and resulting secondary lands, *Climatic*
771 *Change*, 109(1), 117, doi:10.1007/s10584-011-0153-2.
- 772 Ichii, K., H. Hashimoto, R. Nemani, and M. White (2005), Modeling the inter-
773 annual variability and trends in gross and net primary productivity of tropical
774 forests from 1982 to 1999, *Global and Planetary Change*, 48(4), 274–286, doi:
775 10.1016/j.gloplacha.2005.02.005.

- 776 Keenan, T., I. Baker, A. Barr, P. Ciais, K. Davis, M. Dietze, D. Dragoni, C. M.
777 Gough, R. Grant, D. Hollinger, K. Hufkens, B. Poulter, H. McCaughey,
778 B. Raczka, Y. Ryu, K. Schaefer, H. Tian, H. Verbeeck, M. Zhao, and A. D.
779 Richardson (2012), Terrestrial biosphere model performance for inter-annual
780 variability of land-atmosphere CO₂ exchange, *Global Change Biology*, 18(6), 1971–
781 1987, doi:10.1111/j.1365-2486.2012.02678.x.
- 782 Koven, C. D., W. J. Riley, Z. M. Subin, J. Y. Tang, M. S. Torn, W. D. Collins,
783 G. B. Bonan, D. M. Lawrence, and S. C. Swenson (2013), The effect of vertically
784 resolved soil biogeochemistry and alternate soil c and n models on c dynamics of
785 clm4, *Biogeosciences*, 10(11), 7109–7131, doi:10.5194/bg-10-7109-2013.
- 786 Lamarque, J.-F., T. C. Bond, V. Eyring, C. Granier, A. Heil, Z. Klimont, D. Lee,
787 C. Liouisse, A. Mieville, B. Owen, M. G. Schultz, D. Shindell, S. J. Smith, E. Ste-
788 hfest, J. Van Aardenne, O. R. Cooper, M. Kainuma, N. Mahowald, J. R. Mc-
789 Connell, V. Naik, K. Riahi, and D. P. van Vuuren (2010), Historical (1850–2000)
790 gridded anthropogenic and biomass burning emissions of reactive gases and
791 aerosols: methodology and application, *Atmospheric Chemistry and Physics*,
792 10(15), 7017–7039, doi:10.5194/acp-10-7017-2010.
- 793 Langenbrunner, B., M. S. Pritchard, G. J. Kooperman, and J. T. Randerson (2019),
794 Why does Amazon precipitation decrease when tropical forests respond to increas-
795 ing CO₂?, *Earth's Future*, 7(4), 450–468, doi:10.1029/2018EF001026.
- 796 Lawrence, D. M., G. C. Hurtt, A. Arneth, V. Brovkin, K. V. Calvin, A. D. Jones,
797 C. D. Jones, P. J. Lawrence, N. de Noblet-Ducoudré, J. Pongratz, S. I. Senevi-
798 ratne, and E. Shevliakova (2016), The Land Use Model Intercomparison Project
799 (LUMIP) contribution to CMIP6: Rationale and experimental design, *Geoscientific
800 Model Development*, 9(9), 2973–2998, doi:10.5194/gmd-9-2973-2016.
- 801 Lawrence, P. J., J. J. Feddema, G. B. Bonan, G. A. Meehl, B. C. O'Neill, K. W.
802 Oleson, S. Levis, D. M. Lawrence, E. Kluzek, K. Lindsay, and P. E. Thorn-
803 ton (2012), Simulating the biogeochemical and biogeophysical impacts of tran-
804 sient land cover change and wood harvest in the community climate system
805 model (ccsm4) from 1850 to 2100, *Journal of Climate*, 25(9), 3071–3095, doi:
806 10.1175/JCLI-D-11-00256.1.
- 807 Le Quéré, C., R. M. Andrew, P. Friedlingstein, S. Sitch, J. Hauck, J. Pongratz, P. A.
808 Pickers, J. I. Korsbakken, G. P. Peters, J. G. Canadell, A. Arneth, V. K. Arora,

- 809 L. Barbero, A. Bastos, L. Bopp, F. Chevallier, L. P. Chini, P. Ciais, S. C. Doney,
810 T. Gkritzalis, D. S. Goll, I. Harris, V. Haverd, F. M. Hoffman, M. Hoppema,
811 R. A. Houghton, G. Hurtt, T. Ilyina, A. K. Jain, T. Johannessen, C. D. Jones,
812 E. Kato, R. F. Keeling, K. K. Goldewijk, P. Landschützer, N. Lefèvre, S. Lienert,
813 Z. Liu, D. Lombardozzi, N. Metzl, D. R. Munro, J. E. M. S. Nabel, S.-I. Nakaoka,
814 C. Neill, A. Olsen, T. Ono, P. Patra, A. Perea, W. Peters, P. Peylin, B. Pfeil,
815 D. Pierrot, B. Poulter, G. Rehder, L. Resplandy, E. Robertson, M. Rocher,
816 C. Rödenbeck, U. Schuster, J. Schwinger, R. Séférian, I. Skjelvan, T. Steinhoff,
817 A. Sutton, P. P. Tans, H. Tian, B. Tilbrook, F. N. Tubiello, I. T. van der Laan-
818 Luijkx, G. R. van der Werf, N. Viovy, A. P. Walker, A. J. Wiltshire, R. Wright,
819 S. Zaehle, and B. Zheng (2018), Global carbon budget 2018, *Earth System Science
Data*, 10(4), 2141–2194, doi:10.5194/essd-10-2141-2018.
- 820 Lindsay, K., G. B. Bonan, S. C. Doney, F. M. Hoffman, D. M. Lawrence, M. C.
821 Long, N. M. Mahowald, J. Keith Moore, J. T. Randerson, and P. E. Thornton
822 (2014), Preindustrial-control and twentieth-century carbon cycle experiments
823 with the earth system model cesm1(bgc), *Journal of Climate*, 27(24), 8981–9005,
824 doi:10.1175/JCLI-D-12-00565.1.
- 825 Lombardozzi, D. L., G. B. Bonan, N. G. Smith, J. S. Dukes, and R. A. Fisher
826 (2015), Temperature acclimation of photosynthesis and respiration: A key un-
827 certainty in the carbon cycle-climate feedback, *Geophysical Research Letters*,
828 42(20), 8624–8631, doi:10.1002/2015GL065934.
- 829 Lombardozzi, D. L., Y. Lu, P. J. Lawrence, D. M. Lawrence, S. Swenson, K. W.
830 Oleson, W. R. Wieder, and E. A. Ainsworth (2020), Simulating agriculture in
831 the community land model version 5, *Journal of Geophysical Research: Bioge-
832 sciences*, 125(8), e2019JG005529, doi:10.1029/2019JG005529.
- 833 Mahowald, N. M., J. T. Randerson, K. Lindsay, E. Munoz, S. C. Doney,
834 P. Lawrence, S. Schlunegger, D. S. Ward, D. Lawrence, and F. M. Hoffman
835 (2017), Interactions between land use change and carbon cycle feedbacks, *Global
836 Biogeochemical Cycles*, 31(1), 96–113, doi:10.1002/2016GB005374.
- 837 Marcolla, B., M. Migliavacca, C. Rödenbeck, and A. Cescatti (2020), Patterns and
838 trends of the dominant environmental controls of net biome productivity, *Biogeo-
839 sciences*, 17(8), 2365–2379, doi:10.5194/bg-17-2365-2020.

- 841 Moore, J. K., W. Fu, F. Primeau, G. L. Britten, K. Lindsay, M. Long, S. C. Doney,
842 N. Mahowald, F. Hoffman, and J. T. Randerson (2018), Sustained climate warm-
843 ing drives declining marine biological productivity, *Science*, 359(6380), 1139–1143,
844 doi:10.1126/science.aao6379.
- 845 O’Gorman, P. A. (2015), Precipitation extremes under climate change, *Current
846 Climate Change Reports*, 1(2), 49–59, doi:10.1007/s40641-015-0009-3.
- 847 Oleson, K. W., D. M. Lawrence, G. B. Bonan, M. G. Flanner, E. Kluzek, P. J.
848 Lawrence, S. Levis, S. C. Swenson, P. E. Thornton, A. Dai, M. Decker, R. Dickin-
849 son, J. Feddema, C. Heald, F. Hoffman, J.-F. Lamarque, N. Mahowald, G.-Y. Niu,
850 T. Qian, J. Randerson, S. Running, K. Sakaguchi, A. Slater, R. Stöckli, A. Wang,
851 Z.-L. Yang, X. Zeng, and X. Zeng (2010), Technical description of version 4.0
852 of the Community Land Model (CLM), *Technical Note NCAR/TN-478+STR*,
853 National Center for Atmospheric Research, Boulder, Colorado, USA.
- 854 Pan, S., J. Yang, H. Tian, H. Shi, J. Chang, P. Ciais, L. Francois, K. Frieler,
855 B. Fu, T. Hickler, A. Ito, K. Nishina, S. Ostberg, C. P. Reyer, S. Schaphoff,
856 J. Steinkamp, and F. Zhao (2019), Climate extreme versus carbon extreme:
857 Responses of terrestrial carbon fluxes to temperature and precipitation, *Jour-
858 nal of Geophysical Research: Biogeosciences*, 125(4), e2019JG005,252, doi:
859 10.1029/2019JG005252.
- 860 Piao, S., X. Wang, K. Wang, X. Li, A. Bastos, J. G. Canadell, P. Ciais, P. Friedling-
861 stein, and S. Sitch (2020), Interannual variation of terrestrial carbon cycle: Issues
862 and perspectives, *Global Change Biology*, 26(1), 300–318, doi:10.1111/gcb.14884.
- 863 Pitman, A. J., N. de Noblet-Ducoudré, F. B. Avila, L. V. Alexander, J.-P. Boisier,
864 V. Brovkin, C. Delire, F. Cruz, M. G. Donat, V. Gayler, B. van den Hurk, C. Re-
865 ick, and A. Volodioire (2012), Effects of land cover change on temperature and
866 rainfall extremes in multi-model ensemble simulations, *Earth System Dynamics*,
867 3(2), 213–231, doi:10.5194/esd-3-213-2012.
- 868 Poveda, G., A. Jaramillo, M. M. Gil, N. Quiceno, and R. I. Mantilla (2001), Sea-
869 sonally in enso-related precipitation, river discharges, soil moisture, and veg-
870 etation index in colombia, *Water Resources Research*, 37(8), 2169–2178, doi:
871 10.1029/2000WR900395.
- 872 Reichstein, M., M. Bahn, P. Ciais, D. Frank, M. D. Mahecha, S. I. Seneviratne,
873 J. Zscheischler, C. Beer, N. Buchmann, D. C. Frank, D. Papale, A. Rammig,

- 874 P. Smith, K. Thonicke, M. van der Velde, S. Vicca, A. Walz, and M. Watten-
875 bach (2013), Climate extremes and the carbon cycle, *Nature*, 500(7462), 287–295,
876 doi:10.1038/nature12350.
- 877 Seneviratne, S. I., and M. Hauser (2020), Regional climate sensitivity of cli-
878 mate extremes in cmip6 vs cmip5 multi-model ensembles, *Earth's Future*, p.
879 e2019EF001474, doi:10.1029/2019EF001474.
- 880 Seneviratne, S. I., N. Nicholls, D. Easterling, C. M. Goodess, S. Kanae, J. Kossin,
881 Y. Luo, J. Marengo, K. McInnes, M. Rahimi, M. Reichstein, A. Sorteberg,
882 C. Vera, and X. Zhang (2012), *Changes in Climate Extremes and their Impacts
on the Natural Physical Environment*, pp. 109–230, Cambridge Univ. Press, Cam-
883 bridge, U.K., and New York, [Field, C.B., V. Barros, T.F. Stocker, D. Qin, D.J.
884 Dokken, K.L. Ebi, M.D. Mastrandrea, K.J. Mach, G.-K. Plattner, S.K. Allen, M.
885 Tignor, and P.M. Midgley (eds.)]. A Special Report of Working Groups I and II of
886 the Intergovernmental Panel on Climate Change (IPCC).
- 887 Swann, A. L. S., F. M. Hoffman, C. D. Koven, and J. T. Randerson (2016), Plant
888 responses to increasing CO_2 reduce estimates of climate impacts on
889 drought severity, *Proceedings of the National Academy of Sciences*, 113(36),
890 10,019–10,024, doi:10.1073/pnas.1604581113.
- 891 Williams, I. N., M. S. Torn, W. J. Riley, and M. F. Wehner (2014), Impacts of cli-
892 mate extremes on gross primary production under global warming, *Environmental
893 Research Letters*, 9(9), 094,011, doi:10.1088/1748-9326/9/9/094011.
- 894 Wu, Z., E. K. Schneider, B. Kirtman, E. Sarachik, N. Huang, and C. J. Tucker
895 (2008), The modulated annual cycle: An alternative reference frame for climate
896 anomalies, *Climate Dynamics*, 31, 823–841, doi:10.1007/s00382-008-0437-z.
- 897 Xian, G. Z., T. Loveland, S. M. Munson, J. E. Vogelmann, X. Zeng, and C. J.
898 Homer (2020), Climate sensitivity to decadal land cover and land use change
899 across the conterminous United States, *Global and Planetary Change*, 192,
900 103,262, doi:10.1016/j.gloplacha.2020.103262.
- 901 Xu, M., S. Mahajan, F. M. Hoffman, and X. Shi (2019), Evaluating carbon extremes
902 in a coupled climate-carbon cycle simulation, in *Proceedings of the 2019 IEEE In-
903 ternational Conference on Data Mining Workshops (ICDMW 2019)*, pp. 303–310,
904 Institute of Electrical and Electronics Engineers (IEEE), Conference Publishing
905 Services (CPS), doi:10.1109/ICDMW.2019.00052.

- 907 Zhang, T., M. Xu, Y. Xi, J. Zhu, L. Tian, X. Zhang, Y. Wang, Y. Li, P. Shi, G. Yu,
908 X. Sun, and Y. Zhang (2014), Lagged climatic effects on carbon fluxes over three
909 grassland ecosystems in China, *Journal of Plant Ecology*, 8(3), 291–302, doi:
910 10.1093/jpe/rtu026.
- 911 Zhu, Z., S. Piao, R. Myneni, M. Huang, Z. Zeng, J. Canadell, P. Ciais, S. Sitch,
912 P. Friedlingstein, A. Arneth, C. Cao, L. Cheng, E. Kato, C. Koven, Y. Li, X. Lian,
913 Y. Liu, R. Liu, J. Mao, and N. Zeng (2016), Greening of the earth and its drivers,
914 *Nature Climate Change*, 6, doi:10.1038/nclimate3004.
- 915 Zscheischler, J., M. Reichstein, J. von Buttlar, M. Mu, J. T. Randerson, and M. D.
916 Mahecha (2014), Carbon cycle extremes during the 21st century in cmip5 models:
917 Future evolution and attribution to climatic drivers, *Geophysical Research Letters*,
918 41(24), 8853–8861, doi:10.1002/2014GL062409.
- 919 Zscheischler, J., S. Westra, B. J. Van Den Hurk, S. I. Seneviratne, P. J. Ward,
920 A. Pitman, A. Aghakouchak, D. N. Bresch, M. Leonard, T. Wahl, and X. Zhang
921 (2018), Future climate risk from compound events, *Nature Climate Change*, 8(6),
922 469–477, doi:10.1038/s41558-018-0156-3.

923 **Supplementary Material**

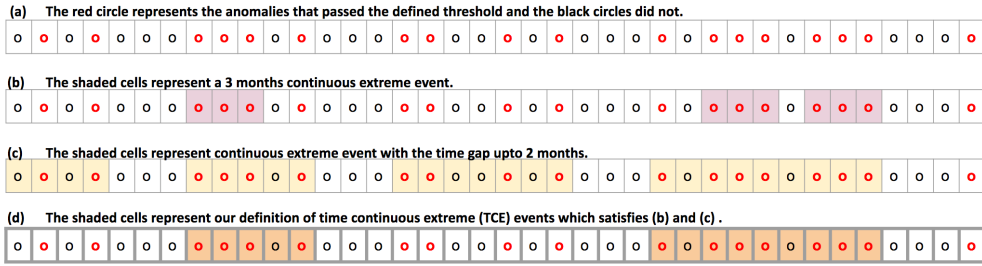


Figure S1: The schematic flow-diagram for finding a temporally contiguous extreme (TCE) event from a time series of variable anomalies at any grid cell. The black and red colored circles represent the anomalies that have not passed and passed the thresholds, respectively. Hence, red circles are individual extreme months in a time series of a variable anomalies (a). We then look for 3 month continuous extremes (b) which is the first condition to qualify as a TCE event. We also look for the individual or temporally continuous extremes that are located in vicinity of each other up to 2 months (c). The temporally contiguous extreme events that fulfil both conditions (shown in (b) and (c)) are referred to as TCE events.

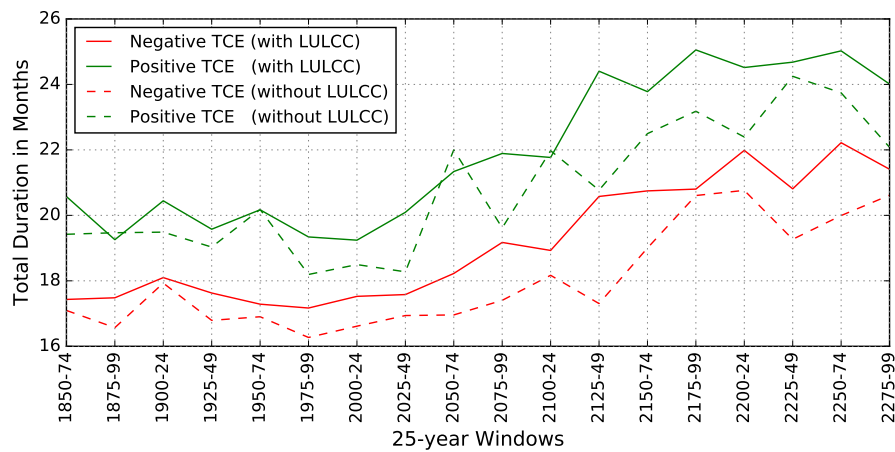


Figure S2: The standard deviation duration of temporally continuous extreme (TCE) events for every time window from 1850–2299. The figure shows the development of standard deviation duration of positive (shown in green) and negative (shown in red) TCEs for both the simulations, *with* (solid lines) and *without* LULCC (dashed lines).

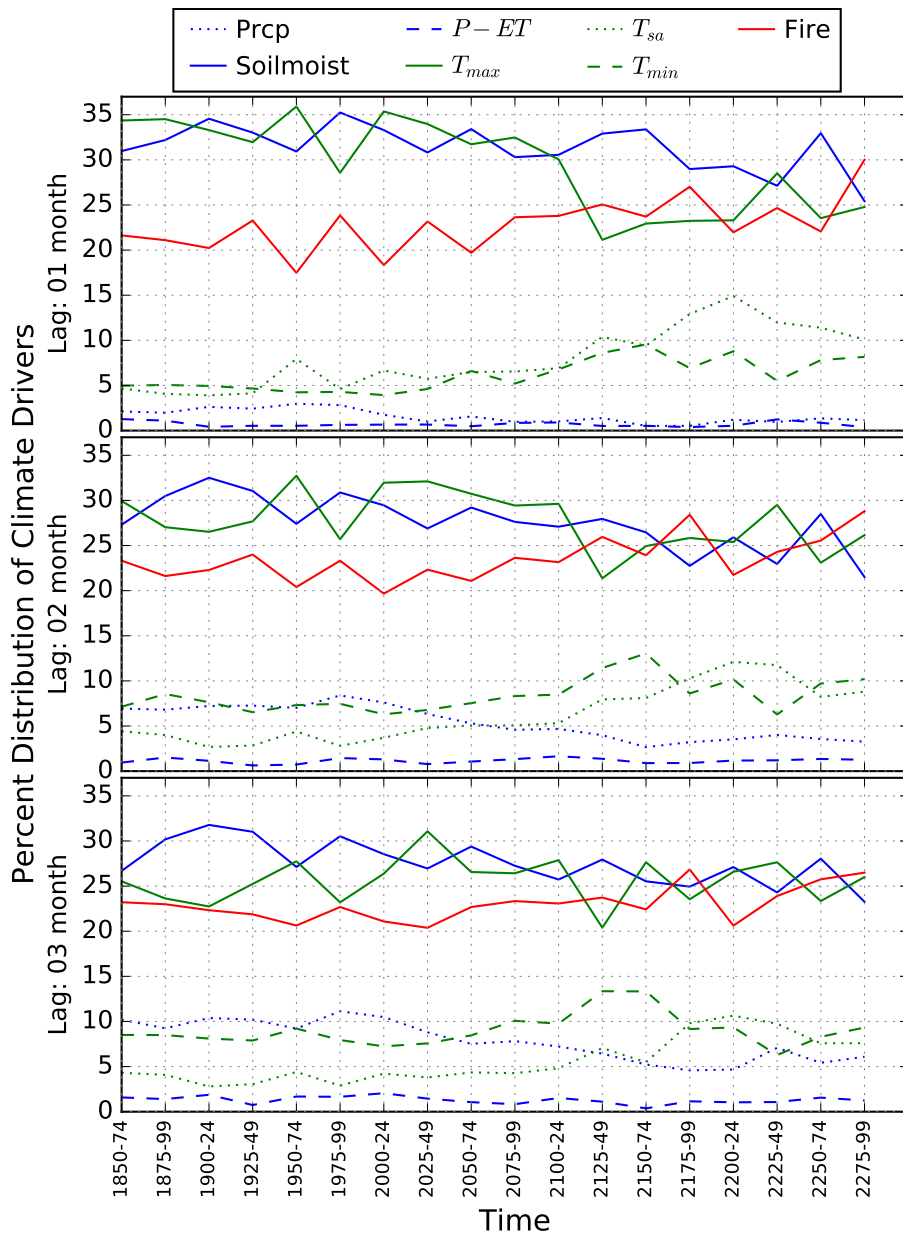


Figure S3: Percent distribution of global dominant climate drivers *without LULCC* for every time window from 1850–2299. For a particular lag month (1, 2, 3, etc.), a climate driver with highest correlation coefficient ($p < 0.05$) with carbon cycle TCEs at any grid cell is called a dominant climate driver.

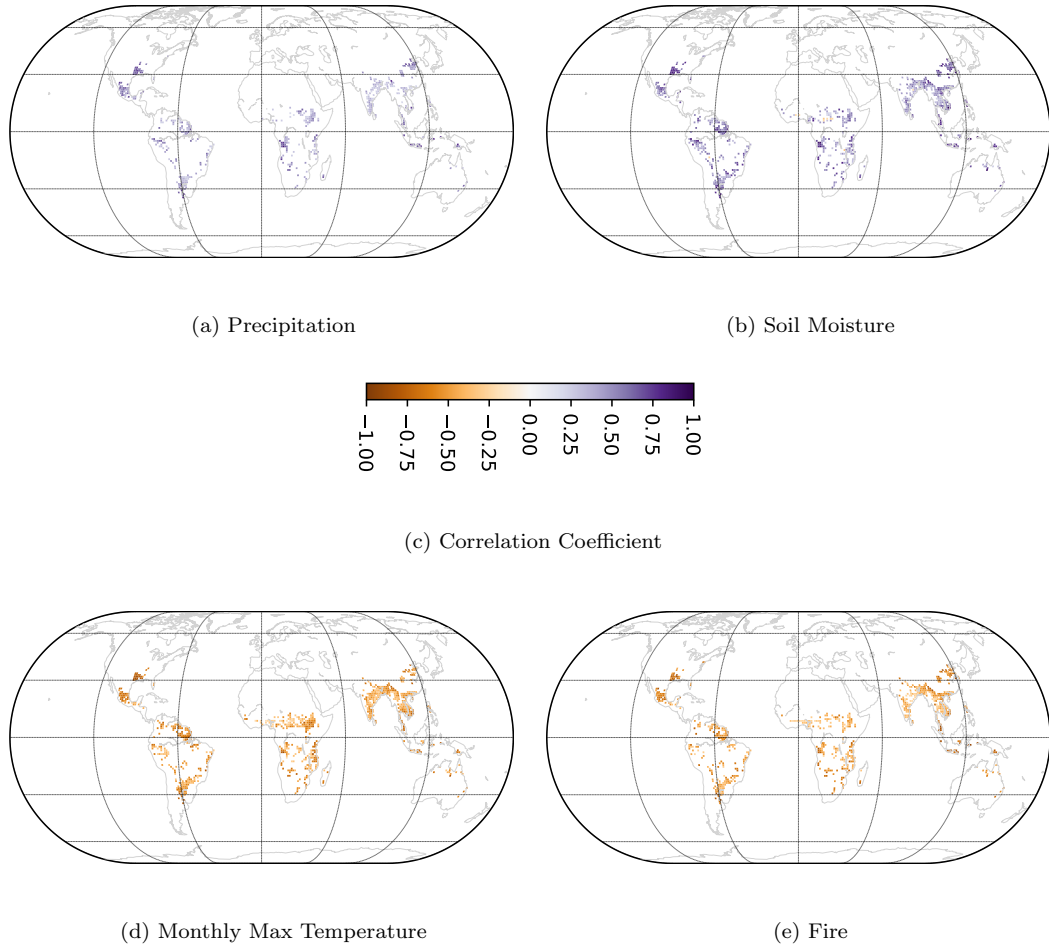


Figure S4: Spatial distribution of climate drivers driving temporally continuous extremes in GPP at a lag of 1 month for the time window 2000–24 for *with LULCC*. Large losses in carbon uptake or increase in negative extremes, and reduction of precipitation and soil moisture are positively correlated. And, increase in temperatures and fire are negatively correlated with negative extremes in GPP. The compound effect of these climate drivers are shown in RGB maps (Figure 7).

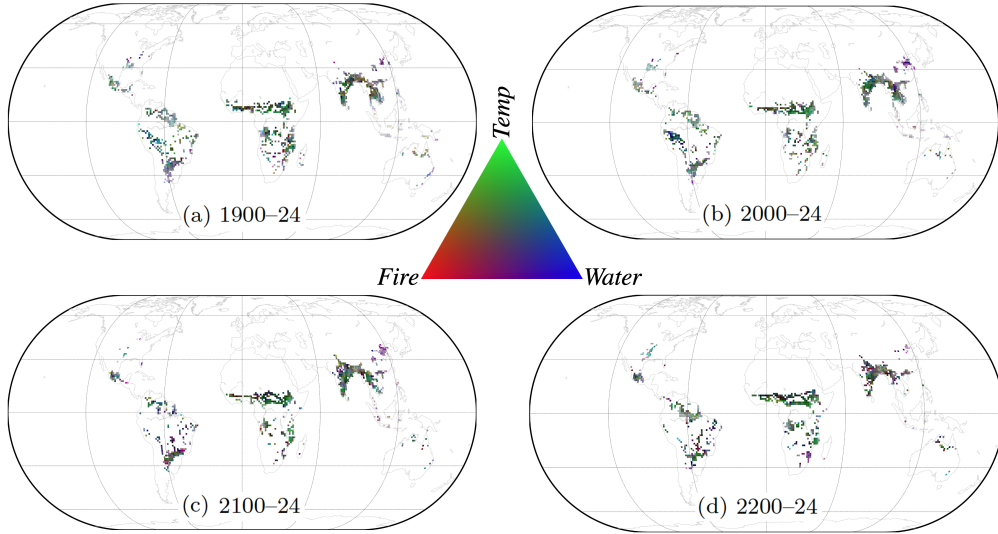


Figure S5: Spatial distribution of climate drivers attributing to negative TCEs for *without LULCC* for four 25-year time windows, (a) 1900–24, (b) 2000–24, (c) 2100–24, and (d) 2200–24. The climate drivers are pooled in three colors, red, green, and blue. Red (*Fire*) is for loss of carbon due to fire, green (*Temp*) represents monthly maximum, mean, and minimum daily temperatures (T_{\max} , T_{sa} , T_{\min} respectively), Blue (*Water*) includes monthly means of soil moisture, precipitation and $P-E$ (precipitation minus evapotranspiration). The results shown here are at 1 month lag.

Table S1: ILAMB score of the variables of CESM1(BGC)

Source: <https://www.ilamb.org/CMIP5/historical/>

Variable/Benchmark Data	IAV Score	Overall Score
Surface Air Temperature/CRU	0.821	0.782
Diurnal Max Temperature/CRU	0.793	0.752
Precipitation/ GPCC	0.793	0.651
Terrestrial Water Storage Anomaly/GRACE	0.905	0.588
Burned Area/GFED4S	0.447	0.409
Evapotranspiration/MODIS	0.617	0.588

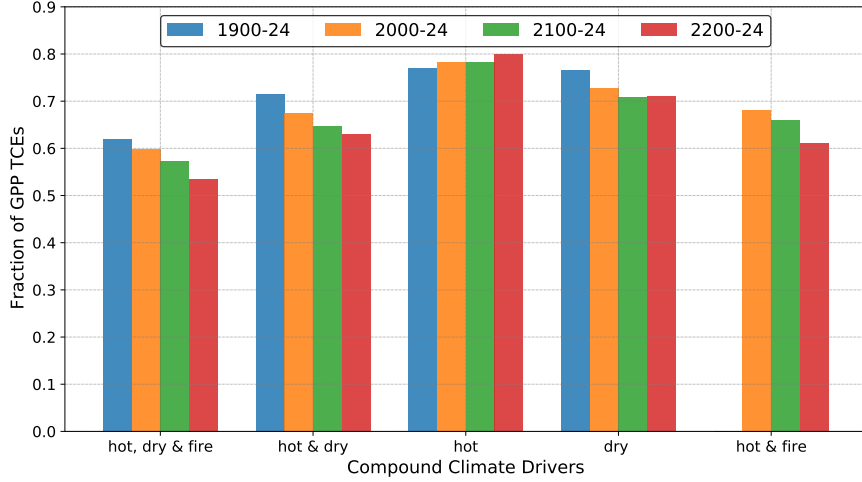


Figure S6: Attribution of temporally continuous extreme events in GPP to compound effect of climate drivers for *with LULCC* at lag of 1 month for 25-year time windows, (a) 1900–24, (b) 2000–24, (c) 2100–24, and (d) 2200–24. The fractions are mutually inclusive, i.e., events driven by *hot and dry* climate is also counted in either *hot* or *dry* climate driven events. Any location could be affected by one or compound climatic conditions. The chart here only represents the inclusiveness of the climatic conditions represented in Figure 8. The combined effect of hot and dry climate accompanied by fire leads to most negative TCE events in GPP.

Table S2: Details of GPP TCEs and PFT distribution at Chaco Province, Argentina. The results are shown for *without LULCC* and time window 2000–24. PFT refers to plant functional type, BDT is broadleaf deciduous tree, and BET is broadleaf evergreen tree.

TCE - neg	TCE - pos	TCE length - neg	TCE length - pos	TCE length - total
5 (events)	7 (events)	40 (months)	53 (months)	93 (months)
PFT (I)	PFT(II)	PFT(III)	Latitude	Longitude
BDT Temperate (43.2%)	BET Temperate (17.91%)	C ₃ grass (17.48%)	25.916° S	300° E

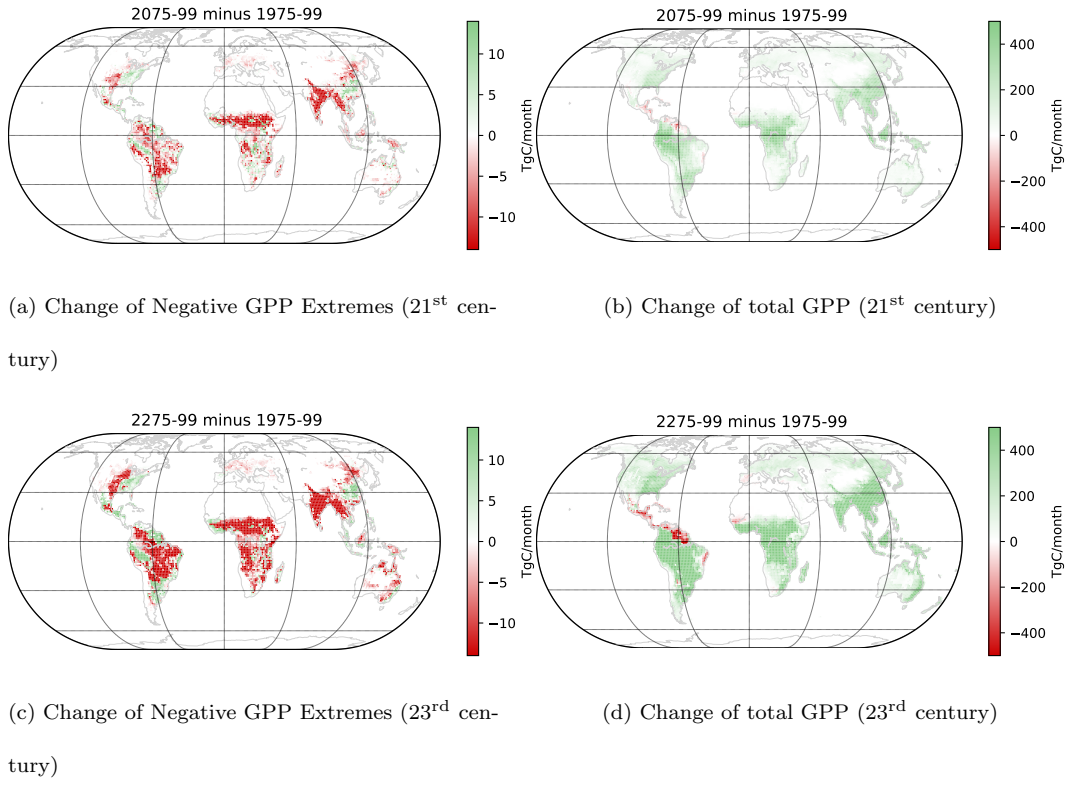


Figure S7: The GPP negative extremes in *without LULCC* (a)&(c) and GPP (b)&(d) are integrated over the whole globe and 25-year time periods. Red and green color in (a)&(c) indicates the increasing and weakening intensity of negative extremes respectively. Red and green color in (b)&(d) indicates the loss and increase of vegetation respectively.

Table S3: Linear regression results for attribution analysis using the cumulative lagged effects for the region of Chaco Province, Argentina. The results are shown for *without LULCC* and time window 2000–24.

Lags	Fire		$P - E$		Precipitation		Soil Moisture		T_{\max}		T_{\min}		T_{sa}	
	CC	PV	CC	PV	CC	PV	CC	PV	CC	PV	CC	PV	CC	PV
1	-0.65	1.76E-12	0.365	3.27E-04	0.557	6.56E-09	0.734	5.85E-17	-0.677	8.89E-14	-0.328	1.31E-03	-0.576	1.54E-09
2	-0.653	1.25E-12	0.479	1.16E-06	0.653	1.25E-12	0.678	8.61E-14	-0.693	1.42E-14	-0.35	5.86E-04	-0.592	4.29E-10
3	-0.647	2.44E-12	0.502	2.99E-07	0.669	2.24E-13	0.639	5.61E-12	-0.676	1.02E-13	-0.364	3.36E-04	-0.585	7.16E-10
4	-0.624	2.45E-11	0.4918	5.53E-07	0.673	1.50E-13	0.621	3.26E-11	-0.674	1.37E-13	-0.36	3.96E-04	-0.584	7.97E-10

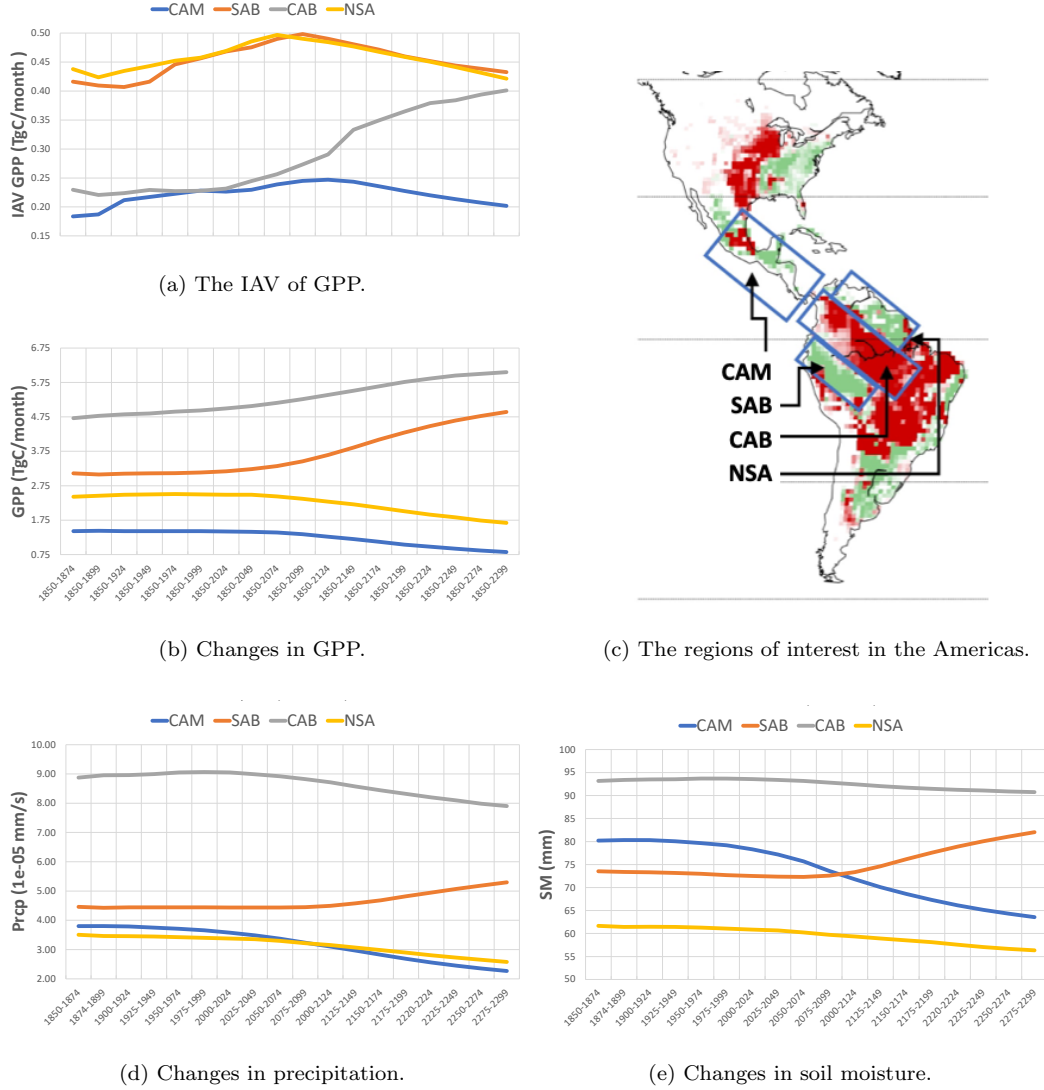


Figure S8: The IAV of GPP and changes in GPP and climate drivers are shown for *without LULCC*. The IAV and changes are calculated from 1850 as the base year to 25 year increments, as shown in *x-axis*.

Table S4: Linear regression results for attribution to climate driver triggers (i.e. onset 25% of TCE length) and cumulative lagged effects for the region of Chaco Province, Argentina. The results are shown for *without LULCC* and time window 2000–24.

Lags	Fire		P – E		Precipitation		Soil Moisture		T_{\max}		T_{\min}		T_{sa}	
	CC	PV	CC	PV	CC	PV	CC	PV	CC	PV	CC	PV	CC	PV
1	-0.679	5.08E-05	0.557	1.68E-03	0.718	1.16E-05	0.609	4.49E-04	-0.622	3.12E-04	-0.331	7.93E-02	-0.534	2.84E-03
2	-0.602	5.50E-04	0.595	6.57E-04	0.697	2.71E-05	0.469	1.03E-02	-0.597	6.32E-04	-0.259	1.75E-01	-0.494	6.49E-03
3	-0.518	3.98E-03	0.569	1.29E-03	0.662	9.15E-05	0.361	5.46E-02	-0.527	3.35E-03	-0.207	2.81E-01	-0.424	2.19E-02
4	-0.377	4.39E-02	0.439	1.71E-02	0.605	5.11E-04	0.353	6.05E-02	-0.479	8.51E-03	-0.125	5.19E-01	-0.36	5.53E-02

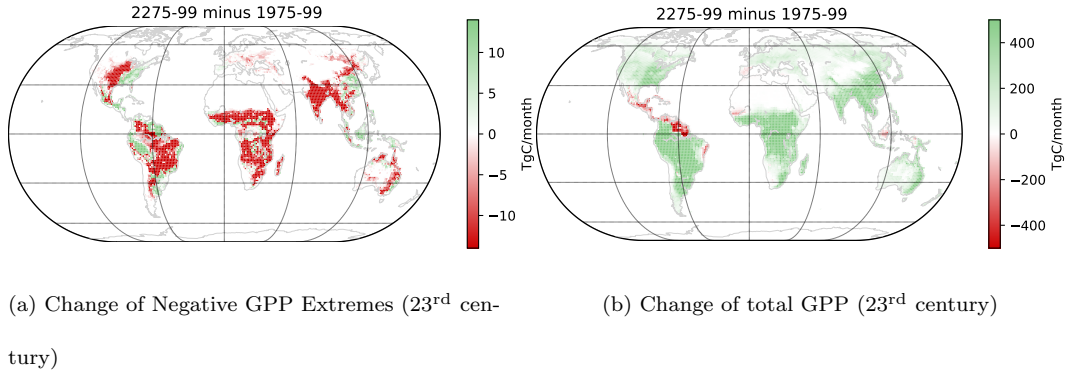


Figure S9: The GPP negative extremes in *with LULCC* (a) and GPP (b) are integrated over the whole globe and 25-year time period. Red and green color in (a) indicates the increasing and weakening intensity of negative extremes respectively. Red and green color in (b) indicates the loss and increase of vegetation respectively. The patterns are similar to the *without LULCC* except for Indonesia which shows the decline of productivity and weakening of negative extreme events.

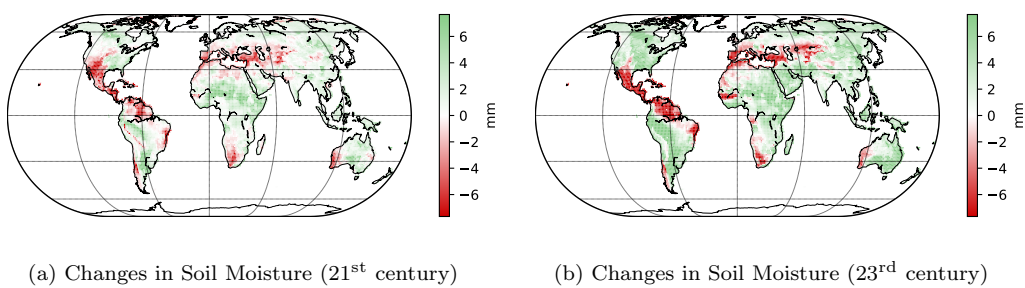


Figure S10: The area weighted average of Soil Moisture for *without LULCC*. (a) Changes in soil moisture for years 2075–2099 minus 1975–1999 and (b) changes in soil moisture for years 2275–2099 minus 1975–1999. Red and green color in indicates the reduction and increase of soil moisture respectively.

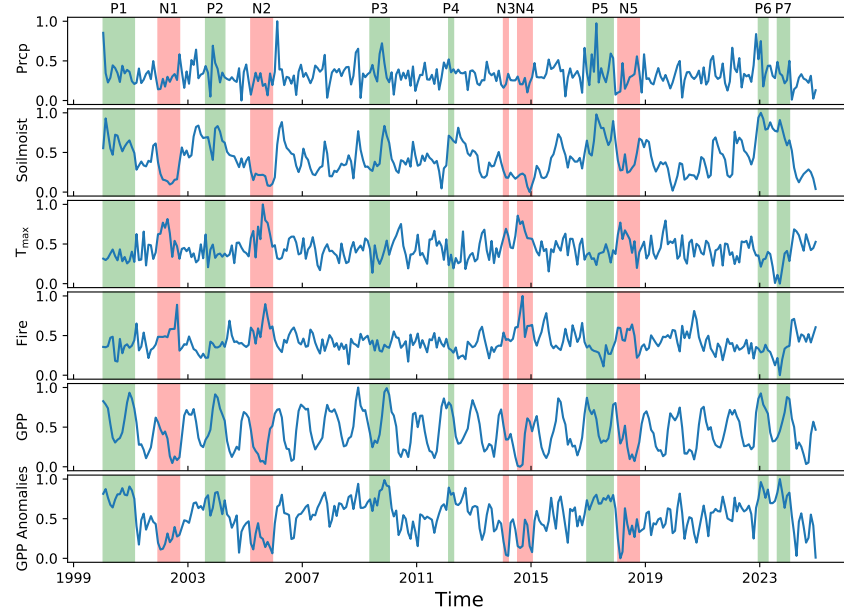
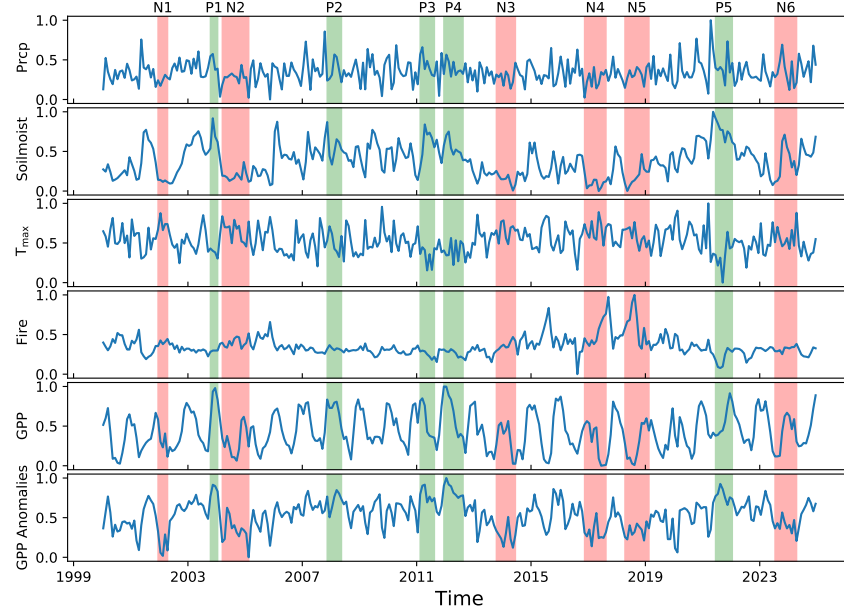
(a) *without LULCC*(b) *with LULCC*

Figure S11: Time series of normalized anomalies of climate drivers and GPP at Chaco Province, Argentina for (a) *without LULCC* and (b) *with LULCC* during 2000–24. The shaded areas in green color span over the positive TCEs ((a): P1 to P7 and (b): P1 to P5). Similarly, the areas in red color represents the negative GPP TCEs ((a): N1 to N5 and (b): N1 to N6).

Table S5: Linear regression results for attribution to climate driver triggers (i.e. onset 25% of TCE length) and cumulative lagged effects for the region of Chaco Province, Argentina. The results are shown for the simulation *with LULCC* and time window 2000–24.

Lags	Fire		$P - E$		Precipitation		Soil Moisture		T_{\max}		T_{\min}		T_{sa}	
	CC	PV	CC	PV	CC	PV	CC	PV	CC	PV	CC	PV	CC	PV
1	-0.457	1.69E-02	0.574	1.74E-03	0.668	1.37E-04	0.549	3.00E-03	-0.73	1.53E-05	0.062	7.57E-01	-0.578	1.59E-03
2	-0.353	7.12E-02	0.598	9.90E-04	0.614	6.47E-03	0.428	2.59E-02	-0.581	1.49E-03	0.056	7.81E-01	-0.418	2.90E-02
3	-0.236	2.37E-01	0.502	7.60E-03	0.512	6.30E-03	0.376	5.33E-02	-0.357	6.75E-02	0.108	5.92E-01	-0.186	3.54E-01
4	-0.2	3.16E-01	0.416	3.09E-02	0.454	1.73E-02	0.367	5.90E-02	-0.293	1.38E-01	0.07	7.28E-01	-0.12	5.50E-01